Universidade de São Paulo
Instituto de Física

Investigação das reações de captura de nêutrons $^{13}C(n,\gamma)^{14}C$ e $^{12}C(n,\gamma)^{13}C$, pelo modelo de potencial

Laura María García Figueroa

Orientador: Prof. Dr. Valdir Guimarães
Coorientadora: Profa. Dra. Marlete Pereira Meira de Assunção

Dissertação de mestrado apresentada ao Instituto de Física da Universidade de São Paulo, como requisito parcial para a obtenção do título de Mestra em Ciências.

Banca Examinadora:
Prof. Dr. Valdir Guimarães - Orientador (IFUSP)
Profa. Dra. Jeannie Rangel (UERJ)
Prof. Dr. Guilherme Soares Zahn (IPEN-CNEN)

São Paulo
2024

FICHA CATALOGRÁFICA
Preparada pelo Serviço de Biblioteca e Informação
do Instituto de Física da Universidade de São Paulo

Figueroa, Laura Maria Garcia

Investigação das reações de captura de neutrons, 13C(n,g)14C e 12C(n,g)13C, pelo modelo de potencial / Investigation of the neutron capture reactions 13C(n, γ)14C and 12C(n, γ)13C, by the potential model. São Paulo, 2024.

Dissertação (Mestrado) - Universidade de São Paulo, Instituto de Física, Depto. de Física Geral.

Orientador: Prof. Dr. Valdir Guimarães
Área de Concentração: Física.

Unitermos: 1. Reações nucleares; 2. Física nuclear; 3. Estrutura da matéria (Física moderna).

USP/IF/SBI-025/2024

Universidade de São Paulo
Instituto de Física

Investigation of the neutron capture reactions $^{13}C(n,\gamma)^{14}C$ e $^{12}C(n,\gamma)^{13}C$, by the potential model

Laura María García Figueroa

Supervisor: Prof. Dr. Valdir Guimarães
Co-supervisor: Prof. Dr. Marlete Pereira Meira de Assunção

Dissertation submitted to the Physics Institute of the University of São Paulo in partial fulfillment of the requirements for the degree of Master of Science.

Examining Committee:
Prof. Dr. Valdir Guimarães - Supervisor (IFUSP)
Prof. Dr. Jeannie Rangel (UERJ)
Prof. Dr. Guilherme Soares Zahn (IPEN-CNEN)

São Paulo
2024

To my husband Chandra.

Acknowledgments

I want to express my deepest appreciation to my supervisor Professor Valdir Guimaraẽs for the opportunity to be part of his group to research in this fascinating field of nuclear physics, for his extensive knowledge and guidance that accompanied me during my master's duration, and for understanding my research interest that made me enjoy all the process to produce this work.

I would also like to extend my gratitude to my co-supervisor professor Marlete Asunção for her endless disposition to help with any question I had and for always providing me with tools to make my work easier.

I am also grateful to the group members of NEAN (Exotic Nuclei and Nuclear Astrophysics) for their valuable advice, suggestions, and experience.

I would like to recognize the assistance of the TANDAR staff for their invaluable contribution and experience during the experimental process.

I gratefully acknowledge the National Council for Scientific and Technological Development (CNPq) for their support through the process 1316685/2021-0.

Thanks should also go to my parents Maria and José, to my brother José Esteban, to my niece Mari Juli and to my nephew Samuel, who always rooted for me and felt proud for my achievements.

Resumo

Esse trabalho consistiu na determinação dos fatores espectroscópicos para os sistemas $<^{12}$C+n$|^{13}$C$>$ e $<^{13}$C+n$|^{14}$C$>$ a partir da análise de Distorted Wave Born Approximation (DWBA) das distribuições angulares para as reações de transferência ^{9}Be(^{13}C,^{12}C)^{10}Be e ^{9}Be(^{13}C,^{14}C)^{8}Be, respectivamente. As medidas das reações de transferência e espalhamento elástico foram realizadas no laboratório Tandar da Argentina em duas energias incidentes E_{Lab} = 55.0 e 62.0 MeV. As distribuições angulares de espalhamento elástico foram analisadas com cálculos de modelo óptico, que descreveram bem os dados experimentais. Os fatores espectroscópicos, obtidos a partir das distribuições angulares das reações de transferência, foram utilizados em conjunto com o modelo de potencial para determinar as seções de choque de captura de nêutrons para as reações ^{12}C(n,γ)^{13}C e ^{13}C(n,γ)^{14}C. Os cálculos para a reação de captura ^{12}C(n,γ)^{13}C foram consistentes com os dados experimentais disponíveis. A seção de choque de captura calculada para a reação ^{13}C(n,γ)^{14}C seguiu aproximadamente a tendência $1/v$ para energias térmicas. Essas reações são importantes nas etapas iniciais da captura lenta de nêutrons que ocorre nas estrelas AGB.

Palavras Chave: Captura de nêutrons, Nucleossintese, DWBA, Modelo Óptico, Fatores Espectroscópicos.

Abstract

This work consisted of determining the spectroscopic factors for the $<^{12}$C+n$|^{13}$C$>$ and $<^{13}$C+n$|^{14}$C$>$ systems through the Distorted Wave Born Approximation (DWBA) analysis of the angular distributions for the transfer reactions ^{9}Be(^{13}C,^{12}C)^{10}Be and ^{9}Be(^{13}C,^{14}C)^{8}Be, respectively. The measurements of the elastic and transfer reactions were carried out at the Tandar laboratory in Argentina at two incident energies, E_{Lab} = 55.0 and 62.0 MeV. The angular distributions of elastic scattering were analyzed with optical model calculations, which described well the experimental data. The spectroscopic factors obtained from the transfer angular distributions were used in association with the potential model to determine the neutron capture cross sections for the ^{12}C(n,γ)^{13}C and ^{13}C(n,γ)^{14}C reactions. Calculations for the ^{12}C(n,γ)^{13}C capture reaction were consistent with available experimental data. The calculated capture cross section for the ^{13}C(n,γ)^{14}C reaction approximately followed the trend of $1/v$ for thermal energies. These reactions are important in the initial steps of the slow neutron capture that occurs in AGB stars.

Keywords: Neutron Capture, Nucleosynthesis, DWBA, Optical Model, Spectroscopic Factors.

List of Figures

List of Tables

Contents

Chapter 1

Introduction

Stellar nucleosynthesis is a fascinating phenomenon in astrophysics responsible for the creation of chemical elements beyond hydrogen and helium. Amid all the different processes and nuclear reactions encompassing the synthesis of elements, there is a kind of reaction of interest for our study: neutron capture reactions. The vast majority of elements heavier than Iron are believed to be synthesized by neutron capture reactions, about half of them by the slow neutron capture or s-process and the other portion by the rapid neutron capture or r-process Iliadis (2015). Both of these processes depend strongly on the availability of free neutrons and their flux. Particularly, the s-process takes place in asymptotic giant branch stars (AGB) (Iliadis, 2015) and massive stars (M$>$ 8$\times$M$_{\odot}$), while the r-process occurs in explosive environments such as supernovae Type-II or neutron merger stars. Understanding the mechanisms involved in these processes aids our comprehension of the stellar evolution and the origin of the elements.

The contribution of nuclear physics to astrophysics is to obtain the values of cross-sections and reaction rates. However, measuring direct neutron capture reactions at astrophysical relevant energies is quite challenging, especially for those reactions involving neutron rich and unstable nuclei. Besides, usually, the cross sections for these reactions, at the low energy regime, are significantly low. For this reason, indirect methods, using more accessible reactions, have been developed to obtain experimental parameters that can be embedded in theoretical tools to calculate the direct capture rates.

In this work, we investigate the neutron capture reactions ^{13}C(n,γ)^{14}C and ^{12}C(n,γ)^{13}C. These reactions are important to define the abundance of the ^{13}C nucleus which plays an

essential role in AGB stars. The reaction ^{13}C(α,n)^{16}O is one of the most important primary neutron sources in the AGB stars (Iliadis, 2015). While the ^{12}C(n,γ)^{13}C neutron capture reaction produces ^{13}C, the ^{13}C(n,γ)^{14}C is considered to be a neutron poison for the slow neutron capture process (Iben and Renzini, 1982), reducing the availability of neutrons. Neutron capture reactions by light nuclei are also important to generate the seeds for the r-process in kilonova (neutron star mergers) and supernova explosions. In the Figure 1.1 we show the reaction flow to produce carbon isotopes. Once formed, these carbon isotopes quickly convert to heavier seed nuclei (Terasawa et al., 2001).

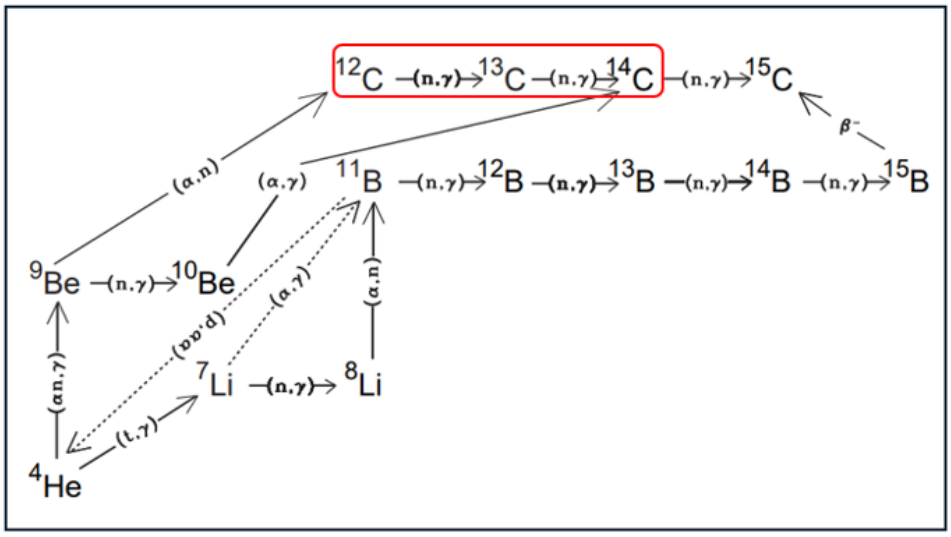

Figure 1.1: Main reaction pathways involving neutron capture reactions in the light nuclei region as seed for the r-process. The reactions involving the carbon isotopes are highlighted (Terasawa et al., 2001)

This work embarks on an exploration of the neutron transfer reactions ^{9}Be(^{13}C,^{14}C)^{8}Be and ^{9}Be(^{13}C,^{12}C)^{10}Be to determine the spectroscopic factors for the $S_{^{13}C+n}$ and $S_{^{12}C+n}$ systems. These spectroscopic factors are obtained from the analysis of the corresponding angular distributions by applying the Distorted Wave Born Approximation (DWBA) calculations. Once these factors are in hands we can employ them to calculate the cross sections of the neutron capture reactions ^{13}C(n,γ)^{14}C and ^{12}C(n,γ)^{13}C, within the Potential Model, aided by RADCAP code Bertulani (2003)

Studies involving the elastic scattering ^{9}Be(^{13}C,^{13}C)^{9}Be (Marzhan Nassurlla et al., 2021) and the neutron transfer ^{9}Be(^{13}C,^{12}C)^{10}Be (Ertao et al., 2017), (Li et al., 2013)

were already found in the literature with energies very close to those of our investigation. In the study by Li et al. (2013), the spectroscopic factor $S_{^9Be+n}$ was calculated from the angular distribution of ^{9}Be(^{13}C,^{12}C)^{10}Be, the same angular distribution we need to obtain $S_{^{12}C+n}$. The elastic scattering ^{9}Be(^{13}C,^{13}C)^{9}Be in Ertao et al. (2017) was studied in a broad range of energies, including energies close to our interest, and for our study it will be advantageous to find an appropriate potential to perform calculations for both the optical model and DWBA.

The experiment to obtain the angular distributions for the elastic scattering ^{9}Be(^{13}C,^{13}C)^{9}Be and the neutron transfer reactions ^{9}Be(^{13}C,^{14}C)^{8}Be and ^{9}Be(^{13}C,^{12}C)^{10}Be was performed at the tandem accelerator TANDAR, which belongs to the Argentine National Atomic Energy Commission (CNEA), situated at the Centro Atómico Constituyentes in Buenos Aires, Argentina. The measurements were carried out using a ^{13}C beam on ^{9}Be target at energies well above the 5.82 MeV of the Coulomb barrier (E_{Lab} = 55.0 and 62.0 MeV).

This dissertation is arranged in such a way that in chapter 2 we briefly introduce nucleosynthesis processes drawing attention to those beyond the iron peak where the neutron capture is involved. Additionally, we review the theoretical methods used to calculate relevant properties such as spectroscopic factors, angular distributions, and cross-sections. Chapter 3 describes our experimental setup. Chapters 4 and 5 are dedicated to the calculation of the angular distributions from the experimental data and the data analysis with theoretical tools, respectively. Our findings are discussed in Chapter 6 referent to our conclusions and lastly, we have added the inputs for our theoretical calculations in the appendix section.

Chapter 2

Theoretical Framework

Since the beginning of the universe, after the Big Bang, all the matter that we see around us (composed of elements heavier than A=6) has been produced in stars. From the oxygen and nitrogen in the air we breathe to the gold on our wedding rings, are all products of a process called nucleosynthesis. This process of element formation, which occurs in stars, is driven by nuclear reactions involving nucleons and other particles and has been happening in the cosmos at different sites and time. The first part of this chapter will be dedicated to briefly reviewing these processes, as part of our research motivation. In particular, we are highlighting the process related to neutron capture, since that is the interest of the present work. The second part of the chapter will be devoted to a review of the theoretical tools used to analyze angular distributions for transfer reactions and how we can obtain spectroscopic information useful to obtain the rates of neutron capture reactions.

2.1 Nucleosynthesis and the Origin of the Nuclides in Nature

The nucleosynthesis of elements includes different processes that occur in various environments and require different sets of conditions depending on the site and time of occurrence: the apparent vacuum of the interstellar medium, minutes after the birth of the universe, the constant generation of radiation from the stars and the explosive and violent events of collapses, collisions, birth, and death of stars (Diehl et al., 2022).

In the 1940's, nuclear physics and cosmology were very active fields of research with the aim to understand the origin of the universe and the chemical elements, especially the lighter ones. However, it was only in the the 1950's that the predominant theory regarding

the formation of the chemical elements in the Universe was developed by G. Burbidge, M. Burbidge, W.A. Fowler, and F. Hoyle. The BBFH theory, as it is called now, postulated that all the elements were produced in stellar interiors or during supernova explosions (Burbidge et al., 1957).

Big Bang Nucleosynthesis (BBN), also known as primordial nucleosynthesis, is the process in which the light species originated: ^{2}H, ^{3}He, ^{4}He (Gamow, 1946) and a portion of ^{7}Li. After the BB the number of neutrons and protons should be approximately the same. However, one second after the BB, this ratio begins to change since neutrons decay into protons, with a half-life of 615 seconds. Actually, without further reactions to preserve neutrons within the stable nuclei, the universe would be pure hydrogen (protons). The reaction that keeps some of the neutrons is the production of deuterium $n + p \rightarrow d + \gamma$. Deuterium is the heavy form of hydrogen (H^2). This reaction is exothermic with a Q_{value} = +2.2 MeV. Nevertheless, at this point, the universe contains billions times more photons (radiation with energy above the 2.2 MeV) than protons, preventing the formation of deuterium until the temperature of the Universe falls to 1 billion K or kT = 0.1 MeV, approximately 100 seconds after the Big Bang. At this time, the neutron-to-proton ratio was about 1 to 7 (Krane, 1988).

After the survival of the deuterium due to the the decrease in radiation energy with the expansion of the universe (and cooling of the temperature), other reactions began to play a role in the production of tritium "t"(^{3}He), ^{4}He, and some ^{7}Li and ^{7}Be:

The light elements ^{1}H and ^{4}He are at the very beginning of the solar abundances, shown in Figure 2.1, and they account for the 98% of the elements in the universe. We can also observe in this figure that there is a region containing light elements such as Li, Be and B, where the abundances drop dramatically. These particular nuclei are not produced by stellar nucleosynthesis, neutron capture processes, or primordial nucleosynthesis. Around 1970 it was proven that these light nuclei were produced by interactions of the galactic cosmic rays with the interstellar medium (Iliadis, 2015). The abundances of these elements were measured in the cosmic rays and the ratio was compared to those from the CNO (Carbon-Nitrogen-Oxygen) cycle elements. The obtained ratio was $\approx 10^6$, which is exactly the one in the solar abundances plot.

Here we are more interested in stellar nucleosynthesis. This is a fundamental astrophysical process that takes place at the core of stars where the elements are synthesized by

a sequence of nuclear reactions. In the stellar interior, the pressure and temperature are high enough to enable the fusion of lighter elements into heavier ones. The stellar nucleosynthesis of the elements can be divided in two types, one synthesizes elements up to the iron peak and the other synthesizes elements beyond the iron peak, see Figure 2.1 for reference. These process happen in the stellar interior and in explosive events, respectively, at different stages of the stellar evolution.

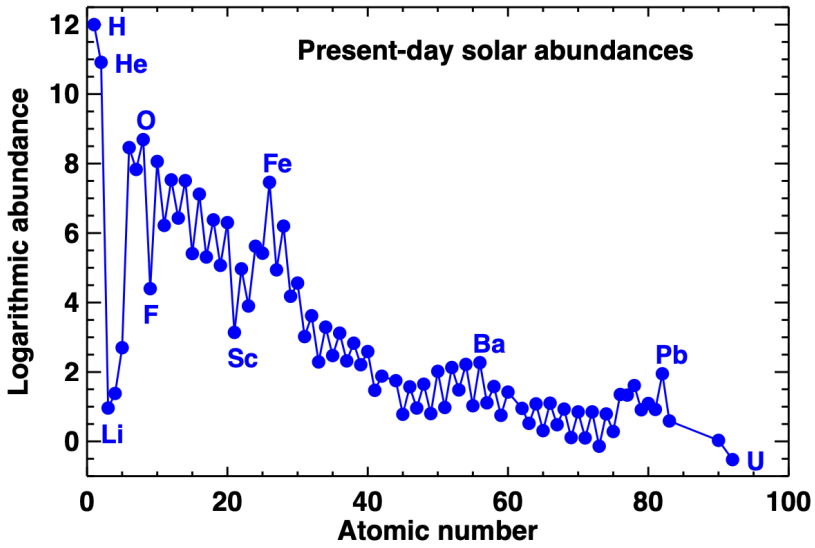

Figure 2.1: Present solar photospheric logarithmic abundances as a function of the atomic number. (Asplund et al., 2021).

The successive processes carried out in the stellar interior during the star evolution, leading up to the synthesis of element in the iron peak, are known as Stellar Burning. These processes refer to the stages in the core of the stars where several consecutive fusion (or capture) reactions take place, leading ultimately to the synthesis of heavier elements up to iron. We will briefly mention each of these stages.

Stellar burning

Hydrogen burning is the first process occurring at the beginning of the star's life, while in the main sequence, and it is the source of its energy. Hydrogen (protons) is the primary component of stars, and in this initial stage, hydrogen undergoes fusion to form helium, facilitated by the heat and pressure in the star's core. The first stars in the universe were mainly composed of the elements helium and hydrogen. Most of them exploded as

supernovae producing new elements that later formed the second generations of stars.

In the first phase of both primary and second generation of stars, the hydrogen is converted to ^{4}He in the interior of the core. This conversion is given by 4H + $2e^-$ $\rightarrow$ ^{4}He + $2\nu_e$. However, this conversion is performed in a sequence of reactions called the p-p (proton-proton) chain reaction, first discovered by Hans Bethe in 1939. The first reaction of the chain is quite complex: as the protons fuse, one of them undergoes beta plus decay, converting into a neutron by emitting a positron and an electron neutrino. Additionally the positron will annihilate with an electron from the environment, producing two gamma rays. At the end, the equation is: $p+p+e^- \rightarrow d+\nu_e+1.442$ MeV. This reaction is dominant in stars with a mass lower or equal to the sun, while the CNO (Carbon-Nitrogen-Oxygen) cycle is believed to be dominant in stars with a mass greater than 1.3 times the mass of the sun. The helium synthesized during this phase accumulates in the star's core, creating the conditions for the next burning phase.

The second phase in the stellar evolution is the helium burning, or Red Giant phase. This phase characterises the more massive stars marking the end of the main-sequence stage. During the hydrogen burning, helium accumulates in the stellar core so, when all hydrogen has been already burned, the helium undergoes nuclear fusion into heavier nuclei like carbon or oxygen through the triple-alpha capture process 2.1. In fact, carbon formation is only possible due to the cluster formation of the $J_\pi=0^+$ resonance at 7.654 MeV in ^{12}C, predicted by Hoyle in 1954 [6]. This resonance, known as the Hoyle state, is responsible for the synthesis of ^{12}C in stars. The observation and confirmation of the existence of this excited state began the investigation of cluster formation in nuclei.

$$\begin{aligned} {}^4He + {}^4He &\rightarrow {}^8Be \\ {}^8Be + {}^4He &\rightarrow {}^{12}C + \gamma \end{aligned} \tag{2.1}$$

Carbon and oxygen are the main products of helium burning so when the helium in the core of the star has been exhausted, the core shrinks due to the gravitational force and the temperature rises to ignite carbon burning. This process takes place in massive stars ($M> 8\times M_\odot$), carbon fuses into heavier elements like neon, magnesium, and sodium.

Only very massive stars (M> 12×$M_\odot$) can continue with the neon burning, where most of the ^{12}C nuclei have been exhausted and the core is mainly composed of ^{16}O, ^{20}Ne, ^{23}Na, ^{24}Mg and ^{20}Ne. Oxygen burning comes after the ^{20}Ne burning due to its smaller alpha separation energy (S_α= 7.162 MeV for ^{16}O and S_α= 4.730 MeV for ^{20}Ne). After all the neon has been depleted, the core is still mostly composed of ^{16}O, ^{24}Mg, and ^{28}Si. Again the core shrinks, the temperature increases, and oxygen burning takes place through the ^{16}O+^{16}O reaction, producing mainly ^{28}Si, ^{32,33,34}S, $^{35,37}Cl$, ^{36,38}Ar and ^{40,42}Ca. At the end of these phases, around 90% of the final composition of the core is ^{28}Si and ^{32}S (Woosley and Heger, 2002).

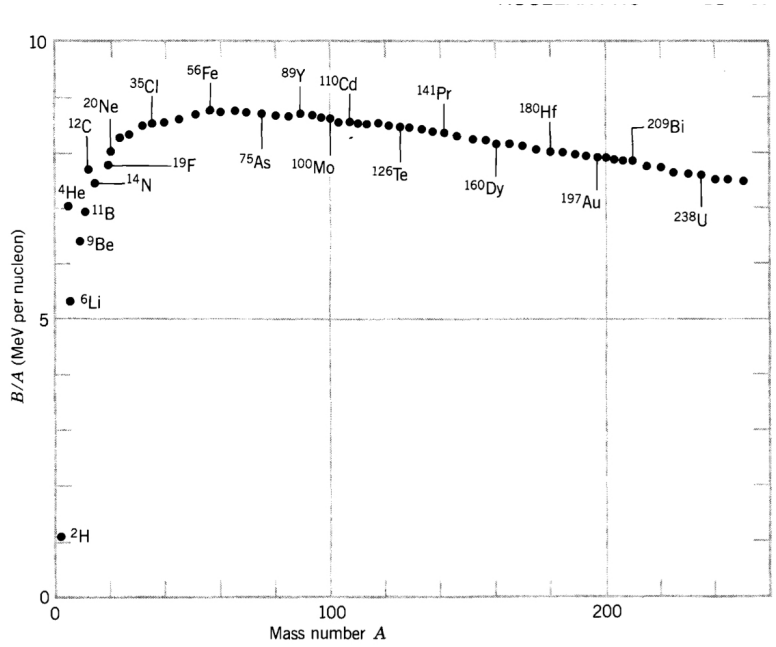

Figure 2.2: Binding Energy per Nucleon. (Krane, 1988)

The stellar core contracts even more, leading to a rise in temperature. However, the high Coulomb barriers of the heavier elements involved now prevent the triggering fusion reactions like ^{28}Si+^{28}Si or ^{28}Si+^{32}S. Alternatively, the nucleosynthesis will be achieved through the photodisintegration of heavier nuclei and the capture of light free particles such as alphas, neutrons, and protons (Iliadis, 2015). In this final stage called silicon burning, the creation of iron will be achieved through successive capture reactions of alpha particles as follows:

$$^{28}\mathrm{Si} + {}^{4}\mathrm{He} \rightarrow {}^{32}\mathrm{S}$$

$$^{32}\mathrm{S} + {}^{4}\mathrm{He} \rightarrow {}^{36}\mathrm{Ar}$$
$$^{36}\mathrm{Ar} + {}^{4}\mathrm{He} \rightarrow {}^{40}\mathrm{Ca}$$
$$^{40}\mathrm{Ca} + {}^{4}\mathrm{He} \rightarrow {}^{44}\mathrm{Ti}$$
$$^{44}\mathrm{Ti} + {}^{4}\mathrm{He} \rightarrow {}^{48}\mathrm{Cr}$$
$$^{48}\mathrm{Cr} + {}^{4}\mathrm{He} \rightarrow {}^{52}\mathrm{Fe}$$
$$^{52}\mathrm{Fe} + {}^{4}\mathrm{He} \rightarrow {}^{56}\mathrm{Ni}$$

After ^{56}Ni, the stellar interior cannot proceed further in fusion reactions. Once ^{56}Ni is formed, it goes to a successive β^+ decay ($^{56}\mathrm{Ni} \rightarrow {}^{56}\mathrm{Co} \rightarrow {}^{56}\mathrm{Fe}$). Also, as can be seen in Figure 2.2, iron is the most efficiently bound nucleus and marks the end of the stellar burning phases.

Nucleosynthesis beyond the iron peak

The synthesis of heavy elements beyond the iron peak in the solar system cannot be explained as a subsequent burning process in the stellar interior, since the abundances found in nature exceed what can be produced under conditions of nuclear statistical equilibrium (Clayton, 1968) where there is a balance between the particles that are emitted due to photodisintegration and the ones that are being captured, thereby preserving the ratios between existing nuclei over time. Thus, there must be a process where there is no restrain of charged particles that increase the Coulomb barrier and requires higher temperatures to trigger fusion. This process can be achieved by the neutron capture. Figure 2.3 shows a schematic representation of the neutron capture process.

Certainly, nucleosynthesis by neutron capture depends upon the availability of neutron density and flux in the environment where the captures take place. Under these conditions there are two such process that can proceed with neutron capture: the slow neutron capture or *s-process* and the rapid neutron capture or *r-process*.

The *s-process* is basically a series of slow neutron capture reaction occurring in an environment with availability of free neutrons. It is called "slow"because of the timing of the neutron capture. This process takes place in a low neutron density and flux. This makes β-decay an important competition for the capture. As the result, the neutron capture occurs with nuclei that are close to the stability valley. The s-process then follows the stability valley and this condition sets its limit to synthesize naturally radioactive elements

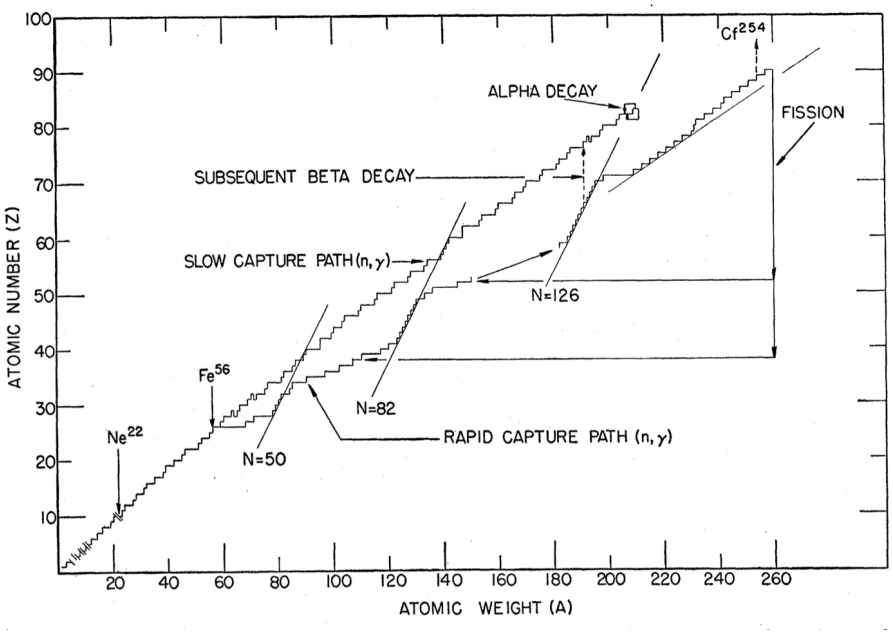

Figure 2.3: Neutron capture paths of the s-process and the r-process (Burbidge et al., 1957)

beyond up to ^{209}Bi (Burbidge et al., 1957). In Figure 2.4 we show the chart of nuclides highlighting the different paths of nucleosynthesis. The cyan arrow indicates the path of the s-process.

The point now is in which environment the s-process takes place. Free neutrons are not exactly available, in a considerable amount, in the interstellar medium. Therefore, the source the neutrons for the s-process should be stellar (Iliadis, 2015). Actually, there are some reactions during the burning stages of stars that release free neutrons in the stellar interior. In particular, in the carbon burning stage in AGB (Asymptotic Giant Branch) stars some reactions can produce a large amount of neutrons, which can be used as fuel to initiate the s-process.

Significant neutron production and s-processing starts with thermal pulses in a star whose core is already composed of carbon and oxygen. These thermal pulses occur when some surface material, such as helium from the outer shell, is convectively mixed deep into the interior of stars where the material has experienced nuclear reactions. As a result, freshly synthesized material is brought to the surface. If these episodes occur during the helium shell burning (AGB-phase), the convective envelope penetrates into the top region of the He-intershell, mixing newly synthesized ^{12}C and s-processed material to the surface

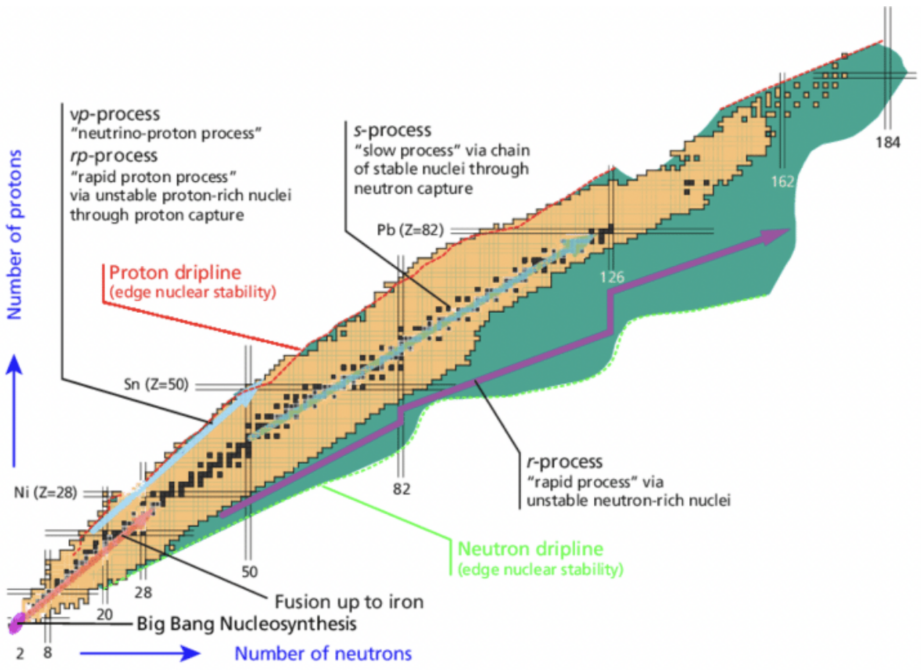

Figure 2.4: Chart of nuclides and the astrophysical processes.

and a few protons into the top layers of the He intershell. These protons are captured by the abundant ^{12}C, thus initiating the sequence ^{12}C(p,γ)^{13}N(β^+)^{13}C in a thin region of the He-intershell, the so-called ^{13}C. Neutrons are produced and released in the pocket under radioactive conditions by the ^{13}C(α,n)^{16}O reaction at temperatures of $\sim$0.9$\times$10^{8}K (Cristallo et al., 2018). At a neutron density of 10^6 to 10^7 cm^{-3}, about 95% of the neutron fluence in AGB stars is reached during this first stage of the s-process because it is restricted to the thin ^{13}C pocket (see the Figure.2.5. The ^{13}C(α,n)^{16}O reaction in the AGB stars strongly depends on the abundance of ^{13}C nucleus. Acquiring information about the direct neutron capture ^{13}C(n,γ)^{14}C and ^{12}C(n,γ)^{13}C is crucial and can offer insights into the s-process, given that these reactions are of importance to create heavy nuclei that are seeds for further neutron captures in the interior of AGB stars.

The fact that the s-process cannot explain the nucleosynthesis of elements beyond ^{209}Bi and the abundances of heavy nuclei with masses around the magic numbers creates the necessity of introducing another mechanism capable of synthesizing elements that are closer to the neutron drip line. This process is known as the *r-process* or rapid neutron capture. Due to the high flux and high neutron density the capture can extend further from the

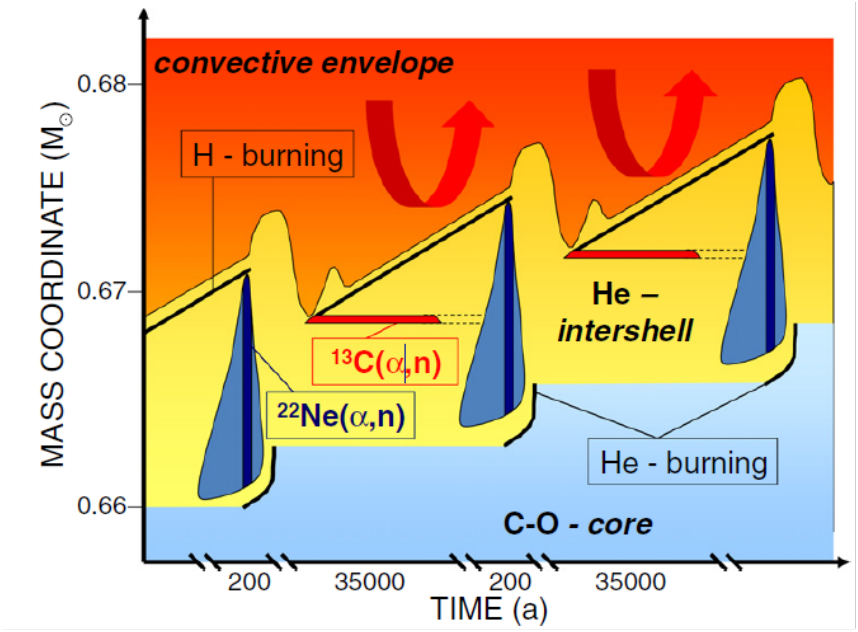

Figure 2.5: Convective Envelope in AGB stars

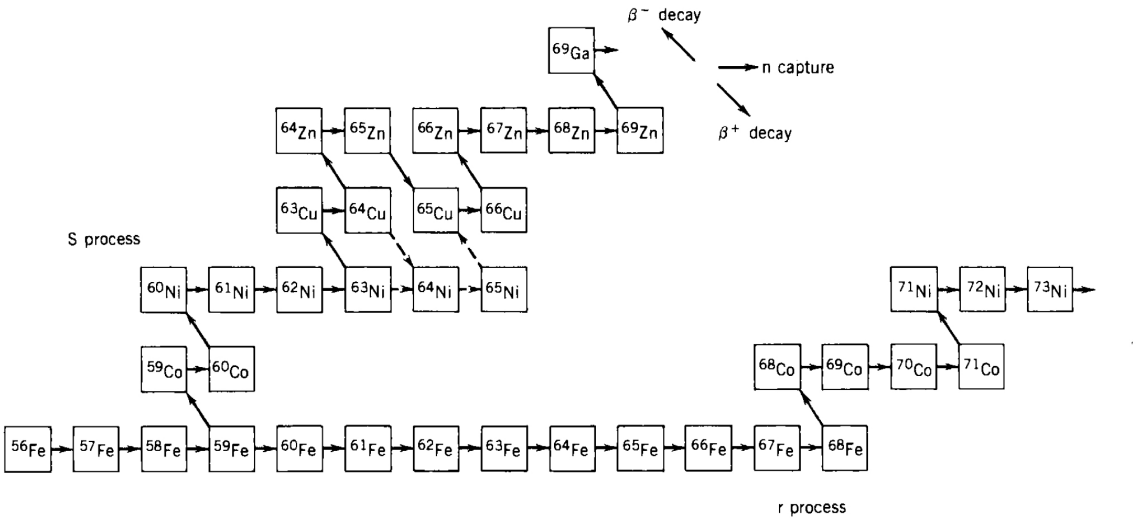

Figure 2.6: Comparison of the path of the s-process and the r-process (Krane, 1988)

valley of stability nuclei, approaching the neutron dripline. The Figure 2.4 shows that the nuclei involved in this process are highly radioactive, with very short lifetime, and the cross section of the reactions following the rapid capture path are very small. Obtaining information on the neutron capture reactions involving these radioactive elements is very important to the understanding of the r-process. However, experimentally, these capture reactions are nearly impossible to be measured in the laboratory. We can have neutron

beam but not target with short lived elements, and we can have beam containing some of these short lived elements but not a pure neutron target. The ideal astrophysical site for the *r-process* is still unclear and subject to debate. A typical scenario requires high neutron densities of 10^{20} cm^{-3} and "moderate" temperatures around 1–2 billion Kelvin to drive the reaction path from the Fe-Ni seeds deep into the neutron-rich region and up to the actinides above U and Th within a few seconds. One of the possible site with these conditions is the core collapse type II supernova explosion. The other potential site is the neutron star mergers, which could also provide the required astrophysical conditions.In this process, the reaction path is dynamically determined by the temperature and the corresponding neutron densities, as well as the timing of the (n,γ) capture and β-decay, which determine the path to very neutron-rich isotopes with one-neutron separation energies of S_n=2–3 MeV. Recently new attention has been drawn to this process thanks to the development of the multi-messenger astronomy, which gathers information from all electromagnetic waves traditionally used in observational astronomy, along with gravitational waves from neutron star mergers. This emerging field of study directly investigates the sites believed to contain a neutron flux large enough to sustain successive neutron captures before the next beta decay occurs in these highly unstable nuclei.

2.2 Theoretical tools for reaction analysis

Since neutron capture reactions, especially by radioactive nuclei, can be quite difficult to be measured directly, several indirect methods have been developed to infer about these captures. Selective direct nuclear reactions, such as breakup and transfer reactions, have been used to investigate and obtain spectroscopic information of the nuclei involved in the collision. In this work we measured the angular distributions for the ^{9}Be(^{13}C,^{14}C)^{8}Be and ^{9}Be(^{13}C,^{12}C)^{10}Be neutron transfer reactions to get information on the spectroscopic factor for the $S_{^{13}C+n}$ and $S_{^{12}C+n}$ systems, respectively. These information led us to calculate the cross sections for the ^{13}C(n,γ)^{14}C and ^{12}C(n,γ)^{13}C neutron capture reactions. In this section we discuss the methods and tools used to proceed with the analysis to obtain the spectroscopic factors and the determination of the capture reactions.

Nuclear reactions are referred to the processes occurring during the collision of two nuclei other than elastic scattering. These processes can reveal properties and mechanisms

in nuclear physics and they play important role in the understanding of the structure and dynamics of the atomic nuclei. In a very general way, two body nuclear reaction can be written as follows:

$$A + a \longrightarrow B + b \tag{2.2}$$

or in a compact way:

$$A(a, b)B \tag{2.3}$$

In this expression, A is the target, a is the projectile, b is the ejectile and B is the recoil or residual nucleus. Depending on the nuclei involved in the interaction, the energy of the incident beam, the impact parameters of the collision and the angles measured, we can get different kind of reactions, from inelastic, transfer and breackup, to fusion, spallation, fragmentation, among others.

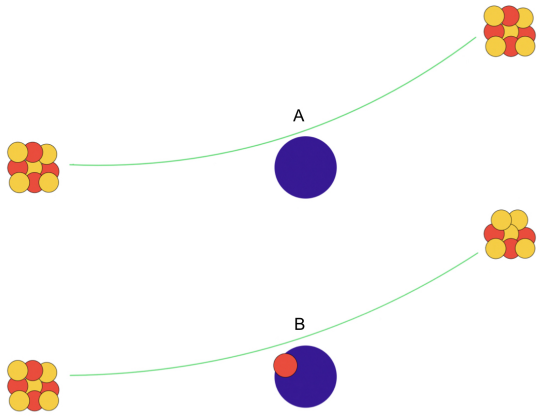

Figure 2.7: Schematic representation of an elastic scattering (A) and a transfer reaction (B)

Elastic Scattering

The elastic scattering is a direct nuclear reaction in which the incident particle interacts with the target nucleus making it to recoil without producing any change in its internal

structure. Total kinetic energy and momentum are conserved throughout the process. An example of an elastic scattering is shown in equation 2.4 and the Figure 2.7A offers a schematic representation.

$$ {}^{1}_{1}p + {}^{A}_{Z}X \longrightarrow {}^{A}_{Z}X + {}^{1}_{1}p \tag{2.4} $$

Inelastic Scattering

In inelastic scattering the interaction between the incident particle and the target nucleus results in the excitation of the target to a higher energy state due to the transfer of energy from the incident particle making the target nucleus to transition to an excited state, what means that the inelastic scattering is a loss of flux from the incident channel. This scattering requires an enough kinetic energy available in the center of mass of the two nucleon system. The equation 2.5 displays an example of an inelastic scattering of neutrons on a nucleus ${}^{A}_{Z}X$.

$$ {}^{1}_{0}n + {}^{A}_{Z}X \longrightarrow {}^{A}_{Z}X^{*} + {}^{1}_{0}n \tag{2.5} $$

Transfer Reactions

Transfer reactions, shown in Figure 2.7 B, involve the exchange of single nucleon or clusters of nucleons between the projectile and the target nucleus incurring in two different scenarios: the projectile nucleus loses one or more nucleons to the target nucleus, called a stripping reaction, and the target nucleus captures one or more nucleons from the projectile, called a pickup reaction. Since it is a peripheral or surface interaction, these reactions are dominant at small angles. Transfer reactions are the main source of spectroscopic information such as energy of resonances or bound states and spin and parity, which can be used to infer about the direct capture cross sections that are difficult to measure directly due to the low energies involved.

2.2.1 Optical Model

A quantitative description of the nucleon-nucleus can be a complicated task, however, if we are interested in the averaged interaction between nucleons in the projectile and in the

target at certain energy, the optical model can be employed through a phenomenological potential that is much simpler (Holt and Whitehead, 2020) adjusting some parameters to fit the experimental data. Thus, we can investigate the average cross section as a function of the incident energy and the mass number. This model considers the interaction between nuclei as intermediate to the interaction predicted by the continuum and the shell models of the nucleus.

In the optical model, the interaction is represented by a complex potential. Here the imaginary part takes into consideration the absorption of the reaction flux by the inelastic channels from the elastic channel, this corresponds to the cross-section of the compound nucleus. As for the real part, it takes account of the potential scattering that is like the one produced by a hard sphere; this whole situation is analogous to the light's processes of scattering and absorption by a medium that has a complex refractive index (Krane, 1988). Both parts of the complex potential, real and imaginary, depend on the energy, in consequence at low energies the real part of the potential is alike to the one in the nuclear shell model and the imaginary part interacts with the incident wave and attenuates it. Due to the fact that the imaginary part of the potential is larger close to the nuclear surface, it is expected that this attenuation will be predominant at the nuclear surface; this situation can be different at higher energies where the absorption of the incident wave may happen uniformly through the nucleus (Roy and Nigam, 1968).

The first form of the optical potential had the shape of a square-well potential

$$U = V(R) + iW(R) \quad \text{for} \quad R < a \tag{2.6}$$

Later, it was observed that the square-well potential overestimated the elastic cross section at the backward angles, this required another form for the potential. Woods and Saxon proposed a modified potential that represents a well with rounded edges that agreed better with the experimental results:

$$U = V(R) + iW(R) \tag{2.7}$$

with

$$V(R) = \frac{V_r}{1 + \exp\left(\frac{R-R_r}{a_r}\right)} \tag{2.8}$$

and

$$W(R) = \frac{V_i}{1 + \exp\left(\frac{R-R_i}{a_i}\right)} \tag{2.9}$$

Where the parameters of the optical potential are V_r, V_i, R_r, R_i, a_r and a_i

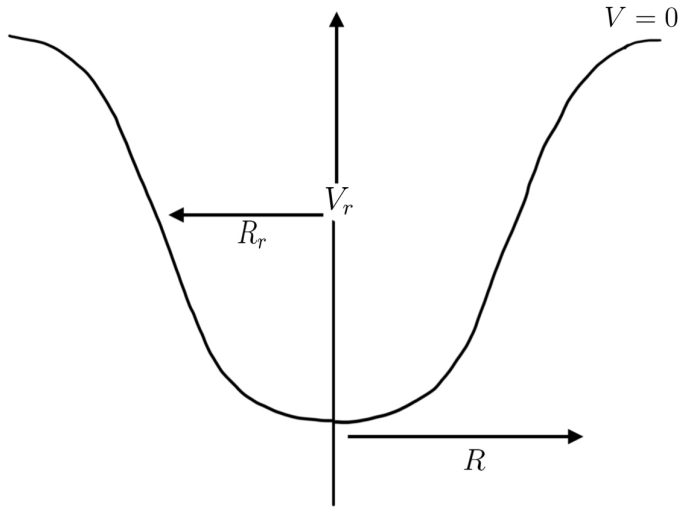

Figure 2.8: Real part of the Woods-Saxon potential)

Figure 2.8 shows the real part of Woods-Saxon potential. R_r is the radius of the equivalent square well, with a value very close to the radius at where the depth of the well is half its central value, a is a surface density parameter.

Other forms of the optical potential besides the one using the Woods-Saxon potential are employed depending on the interactions being studied, especially potentials that better account for the deformation of the nuclei of interest. However, for our analysis,

the potential model with a Woods-Saxon potential is enough as this potential accurately represents the most forward angles of the neutron transfer reactions in the region where they dominate.

2.2.2 *Distorted Wave Born Approximation (DWBA) and Spectroscopic Factors*

Distorted Wave Born Approximation (DWBA) is the most commonly used theoretical tool to calculate the cross section of transfer reactions assuming that for our reaction both entrance and exit channels are dominated by elastic scattering and that the transfer reaction $A(a,b)B$ with $a = b + x$ and $B = A + x$ takes place between the channels $a + A$ and $b + B$. Here, x represents the transferred nucleon. Figure 2.9 shows a schematic representation of the transfer reaction. This reaction can be considered as a first order perturbation and it is a one step-direct reaction, meaning that there is no rearrangement as the nucleon or nucleons are already placed in the final state.

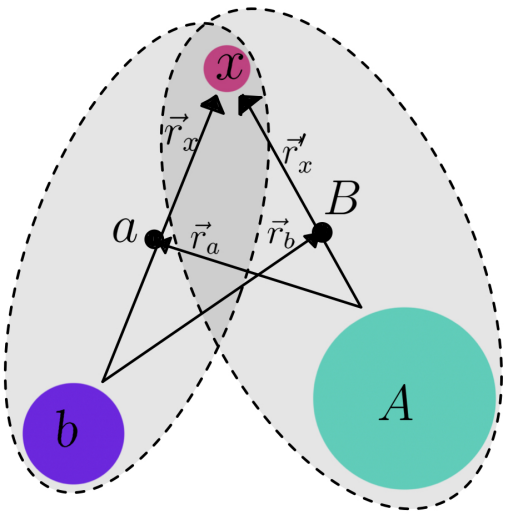

Figure 2.9: Coordinates of a Nuclear Transfer Reaction $A(a,b)B$ with the projectile $a = b+x$ and the exit channel $B = A + x$; x is the transferred nucleon. Figure adapted from NRV (2023)

The cross section of the transfer in the DWBA model is proportional to the squared of the transition matrix T given by Hammache and de Séréville (2021):

$$T_{i\to f}^{\mathrm{DWBA}} = J \iint \chi_f^{(-1)}\left(\vec{k}_f, \vec{r}_f\right)^* \langle b, B \left| V_{bB} - U_{bB} \right| a, A\rangle \, \chi_i^{(+1)}\left(\vec{k}_i, \bar{r}_i\right) d\vec{r}_i d\vec{r}_f \qquad (2.10)$$

For a reaction $A(a,b)B$ we have according to equation 2.10:

- χ_i and χ_f, the distorted wave functions corresponding to the entrance and exit channel respectively
- $\vec{k}$ and $\vec{r}$, the wave number and the channel's relative coordinates
- J, the Jacobian of the transformation of coordinates
- $V_{bB} - U_{bB}$, the non-elastic scattering processes
- V_{bB}, the sum of the interactions between b and B
- U_{bB}, the optical potential describing the elastic scattering of b+B

If the nucleon transferred is small in comparison with the target, the term $V_{bB} - U_{bB}$ can be approximated by the potential V_{bx}^3; we can then write $\langle b, B \left| V_{bx} \right| a, A \rangle$, this quantity is called the form factor of the reaction that contains the information about the nuclear structure. The potential V_{bx} only acts on the projectile thus we can rewrite $\langle b, B \left| V_{bx} \right| a, A \rangle = \langle B \mid A \rangle \langle b \left| V_{bx} \right| a \rangle$; this term also encloses the overlap function $I_{xA}^B(r)$ that describes the transferred nucleon in the final bound state B and it can usually be approximated by equation 2.11 (Hammache and de Séréville, 2021):

$$I_{xA}^B(r) = S_{xA}^{1/2} \varphi_{xA}(r) \tag{2.11}$$

where S_{xA} is the spectroscopic factor of the system $x + A$ and $\varphi_{xA}(r)$ the bound state wave function in the radial direction also of the system $x + A$.

2.2.2.1 Spectroscopic Factors

The spectroscopic factor is defined by a matrix element between the initial state in the entrance channel and the final state of the exit channel, they provide information about the structure of the nuclei in the shell model (Lee et al., 2007). In our transfer reaction A(a,b)B, the spectroscopic factor S_{xA} shows the overlap probability between the wave function of the system $x + A$ and the final bound state configuration B (Hammache and de Séréville, 2021).

Experimentally the spectroscopic factors are calculated by finding the ratio between the experimental cross section and the one calculated using a reaction model, for our analysis we used the DWBA theory 2.12.

$$\left(\frac{d\sigma}{d\Omega}\right)_{\text{exp}} = S_{xA}S_{xb}\left(\frac{d\sigma}{d\Omega}\right)_{DWBA} \tag{2.12}$$

In equation 2.12 we have a normalization factor that contains both spectroscopic factors from the two systems involved in the transfer S_{xA} corresponding to the $x + A$ bound state and S_{xb} corresponding to the final state of the transfer. This expression implies that by knowing the spectroscopic factor of one of the systems, it is possible to calculate the other experimentally.

Chapter 3

Experimental Setup

In this chapter, we will present a description of the experimental setup used in the experiment of this work. The experiment was performed at the TANDAR laboratory, hich is part of the Argentine National Atomic Energy Commission (CNEA). The laboratory is situated within the Centro Atómico Constituyentes in the city of Buenos Aires, Argentina. The ^{13}C beam, delivered by the tandem accelerator at energies of E_{Lab}= 55 and 62 MeV, was impinged on a $2\mu m$ thick ^{9}Be target. As a result of the interaction of these nuclei, several elements from different reactions were produced. We were particularly interested in the ^{13}C+^{9}Be elastic scattering and in the neutron transfer reactions, ^{9}Be(^{13}C,^{12}C)^{10}Be and ^{9}Be(^{13}C,^{14}C)^{8}Be. Below are some details on the setup and laboratory.

3.1 The accelerator

TANDAR is an electrostatic heavy-ion tandem accelerator with a electric tension with nominal value of 20 MV. However, in nowadays the accelerator can reach up to 12 MV. It is accommodated in a 70 m tower. Tandem accelerators incorporate multiple stages for particle acceleration, usually through the use of electrostatic fields, intending to increase the energy of the particles. The initial stage corresponds to the ion production from the ion source, where the particles comprising the beam are extracted. To achieve the desired energies and mass selections as well as to focus the beam, a series of electrical devices are positioned along the line of the accelerator. These devices ensure that only the nuclei of interest, at the desired energy, remain in the beam. After this is achieved, the beam is collimated and delivered to the reaction chamber where the reactions will take place. A schematic drawing and picture of the TANDAR Accelerator are shown in figures 3.1 and

3.2, respectively.

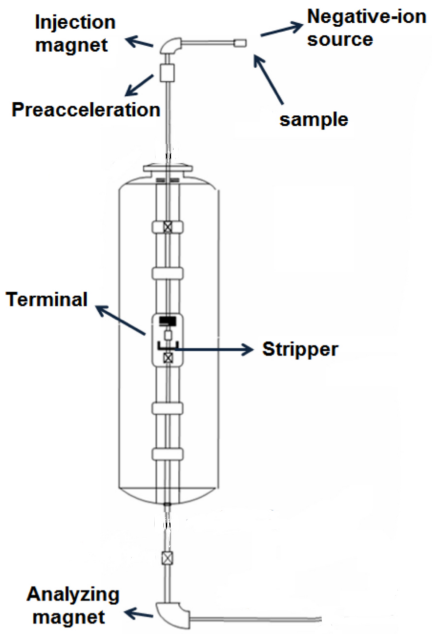

Figure 3.1: Schematic diagram of the heavy ion accelerator TANDAR. Adapted from de Jesús et al. (2019)

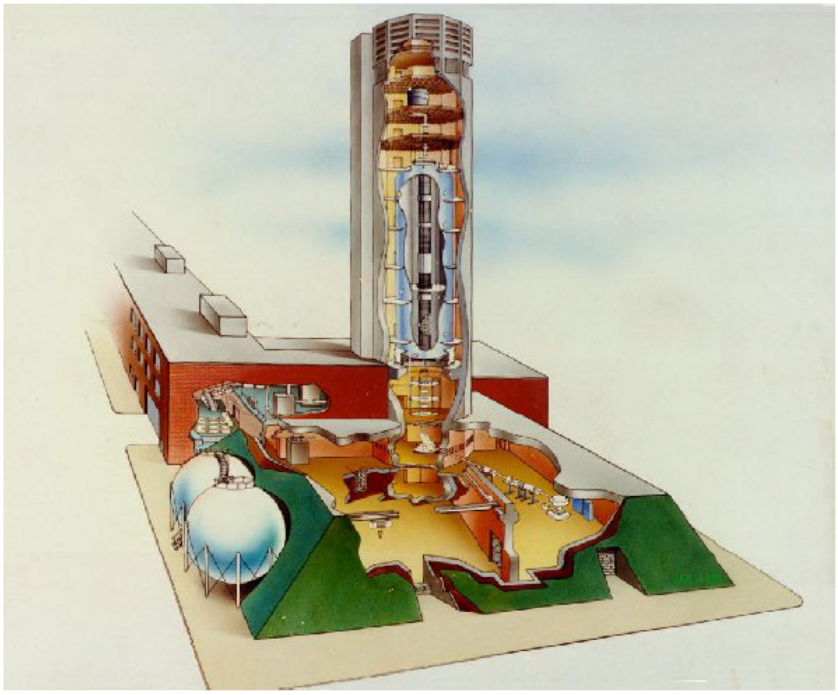

Figure 3.2: Picture of the Tandar Accelerator with the experimental lines

The ^{13}C beam used in this measurement was produced by a source of the MC-SNICS type (Multicathode Source of Negative Ions by Cesium Sputtering), where the beam material of interest is placed on a cathode. Cesium vapor from a reservoir heated to 1200^{o}C is introduced into the source and positively ionized by a filament. This positively ionized cesium is then directed towards the cathode due to a potential difference. When the cesium collides with the cathode material, it causes the extraction and ionization of the material through a process known as sputtering. The ionized beam material of interest is then extracted from the source by a potential difference of 3 kV (extraction voltage). These ions then undergo a pre-acceleration with a voltage of Vp = 12 kV.

After this pre-acceleration, the beam of interest (^{13}C), together with some other elements that are eventually extracted together with the beam, are directed to the ejector magnet to deflect the beam by 90^o. At the same this magnet deflector act also as selecting magnet, deflecting only the element of interest by magnetic rigidity:

$$\rho = \frac{p}{qB} = \frac{\sqrt{2mE}}{qB}, \tag{3.1}$$

where E is the kinetic energy of the beam and, taking into account that all ions have the same energy and charge, the magnet deflector works as mass selector.

The next stage consists of directing the beam to the entrance of the accelerator. As mentioned the acceleration is given in two stages with a high voltage V_T at its midpoint. Initially, the ions enter the accelerator column with charge state $q = -e$, with $e = 1.602 \times 10^{-19}$ C. At this point, in the middle of the acceleration tube, the kinetic energy of the ions is $K = e(V_p + V_T)$. Positioned at this point are the thin carbon foils and the ions pass through it, thereby losing a quantity q of their electrons, changing their charge to $+qe$. After this change of change, the ions become positively charged and there is a second acceleration of these ions towards the ground potential. Here they are once again focused by a second magnet known as analyzer magnet. Not all ions emerge with the same charge after the strip carbon foil. Instead, a distribution of several charge states P(q) is obtained. Due to this dispersion in charge, we also obtain an energy distribution of the particles that enter the magnet analyzer. Thus, the magnet analyzer selects a narrow band of energy centered on the value of interest. In effect, we can calculate the final kinetic energy of the ions after the accelerator itself by the relationship: $K = e(V_p + V_T + eqV_T)$.

There is still a collimating slit (slit-03) positioned at the focus of the analyzer magnet, with the aim of containing contamination with residual gas molecules or particles from collisions with the acceleration tube. Moreover, this final collimator providing also the electric current information generated by the impact of the beam charged particles, and uses it to regulate the voltage of the accelerator terminal, that is, it corrects energy variations of the beam, keeping it constant. This is called beam slit control.

In the TANDAR Laboratory, the analyzer magnet is not fixed. It can move and be attached to different experimental lines. This flexibility allows us to select the experimental line, move the magnet analyzer accordingly, and focus the beam directly into the scattering chamber to be utilized in the experiment. The specific setup within the scattering chamber for the present experiment is described in the following section.

3.2 The setup in the scattering chamber

The ^{13}C beam was directed to the scattering chamber. This chamber has 70 cm of diameter with two rotating plates were we can place the detectors. In figure 3.3 we have a schematic drawing of the chamber with the basic elements of our experimental setup. In the figure 3.4 we show a picture of this chamber. Although, the drawing includes two detectors as monitors, only one of them was used in our experiment. The monitor M_2 was left out to make room for the telescope to be moved to the minimum θ_1 possible. The reason behind this is that we desire to have the cross section for the angular distribution of transfer reactions at the most forward angle, where they are dominant.

The detector system comprised four telescopes, each consisting of two silicon detectors arranged in a sequence (ΔE-E), where the thin detector (ΔE) was 22 μm thick and the thick detectors (E) was 1000 μ m thick. Each telescope was more or less 10° apart of each other. In the Table 3.1, we present the actual angular distances between each telescope as a function of the position of the first telescope, T_1 θ_1. The front detector (ΔE) has to be thin enough to allow all particles of interest to punch through it and continue their trajectories to the second detector, where they will be completely stopped and deposit all of their remaining energy. However, this detector must also be thick enough to dissipate some energy and allow the charge reading. These detectors are a p-n-type silicon diode containing a thin depletion layer that will be depleted depending on the voltage applied.

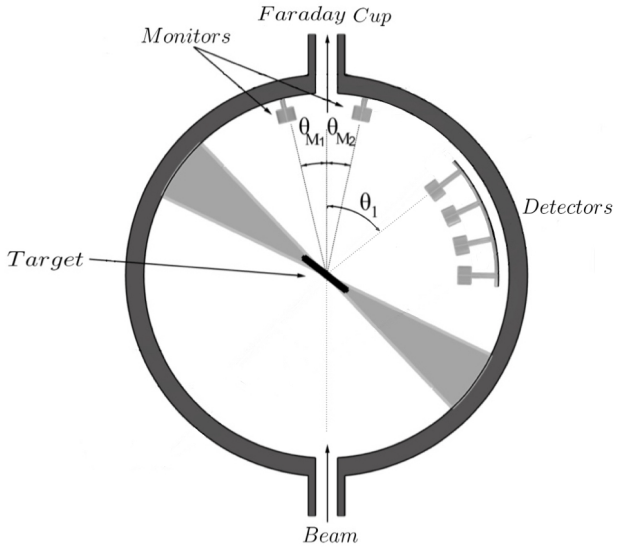

Figure 3.3: Schematic of the reaction chamber. Adapted from Gollan Scilipotti (2019)

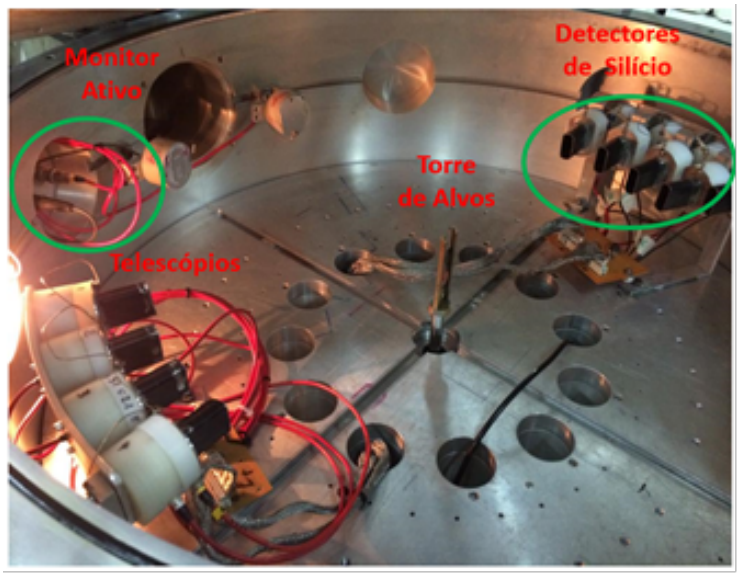

Figure 3.4: Picture of the setup in the scattering chamber

When an incident particle hits the depletion layer, it creates e-h (electron-hole) pairs, and the quantity of these pairs will depend on the characteristics of the detector and will be proportional to the energy of the incident particle. The created h-e pairs move to the corresponding electrode and produces an electric signal proportional to the energy of the incident particle. (Dey and Bhattacharya, 2023).

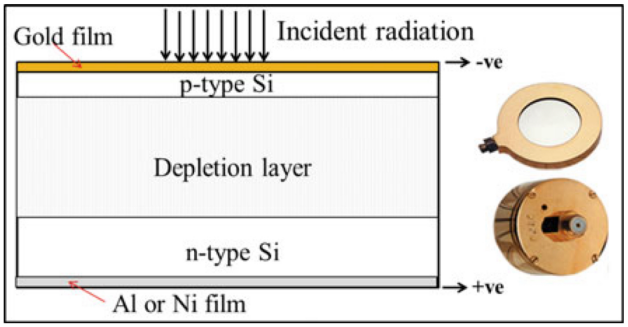

Figure 3.5: Schematic of a silicon detector. Taken from Dey and Bhattacharya (2023)

To treat the electronic signals coming from the detectors on the TANDAR Laboratory, we use the MSI-8 module from Mesytech, which receives the signals proportional to the energy of the detectors in one of the 8 inputs. These signals are subsequently injected into a shaper module, where they are filtered, inverted and then divided into two distinct signals of energy and time (Discriminator Gate Generator). The pulses are still converted into analog pulses before leaving this module. Next, both signals are connected to an ADC (Analog to Digital Converter) where they are digitized through a multichannel controller board and analyzed by the SPMROOT data acquisition interface (which connects the electronic modules to the computer). At the end we have in the computer all the energy spectra in terms of channels read to be calibrated in energy.

The motivation behind using the telescope is to characterize and identify the particles produced by the collision of ^{13}C+^{9}Be from the different reactions. By creating a bi-parametric plot with both (ΔE) and E signals we can distinguish between the different nuclei produced in the reaction. Before conducting the experiment, a simulation of the particle's kinematics and the loss of energy in each detector was performed to ensure that all scattered particles would be stopped at the thick detector. We performed this simulation using the tools *kineq* and *stopx* (Milner, 1986).

We used a $2\mu m$ thick ^{9}Be foil as the target, which was placed at the center of the reaction chamber. This target was rotated by 20° related to the beam direction and kept fixed throughout all experimental runs, same conditions were maintained for both energies measured.

Table 3.1 - Measured angular distance between the telescopes in the holder

T_1	$T_1 - T_2$ (Deg)	$T_2 - T_3$ (Deg)	$T_3 - T_4$ (Deg)
θ_1	9,80	9,52	9,30

3.3 Experimental Procedure

In our experiment, the ^{13}C beam was impinged on a 2μm thick ^{9}Be target in the reaction chamber at E$_{Lab}$= 55 MeV and 62 MeV. The same conditions were maintained for both energies. The idea was to get as many as possible measurements in different angles to build the full angular distributions. Also it was important to get good statistics in each angle. In order to cover the desired angular range, our detector system was moved accordingly. The angular range measured covered by our telescope system was from θ_{Lab}=7.5^o to 47.0^o, in 2.5^o steps. The kinematics limit for the inverse kinematic reaction ^{9}Be(^{13}C,^{13}C)^{9}Be was about θ_{Lab}=43.5^o. Beyond this angle, no elastic particles were observed in the spectra. However, due to the too small cross section, as well, no counts for ^{14}C or ^{12}C from the ^{9}Be(^{13}C,^{14}C)^{8}Be and ^{9}Be(^{13}C,^{12}C)^{10}Be reactions, respectively, were observed beyond θ_{Lab}=30.0^o

Chapter 4

Determination of the Angular distributions

The initial step of the data analysis is the data Reduction. Information and discussions regarding the physical processes of interest for us are obtained and investigated from the theoretical analysis of the measured angular distributions, that is, the cross section as a function of detection angle. However, to come from the detector signals to the angular distributions, we have to perform what we call *data reduction*. In this chapter, we describe the methodology used to reduce the data and obtain the angular distributions of the elastic scattering cross section and transfer reactions. The first step towards reducing the raw data involves the calibration in energy of the spectra. Once we have all the spectra, duly calibrated, we converted them to the ROOT format for further analysis.

This chapter contains the detailed description of the steps to derive the experimental angular distributions corresponding to the elastic scattering ^{13}C+^{9}Be as well as the ^{9}Be(^{13}C,^{12}C)^{10}Be and ^{9}Be(^{13}C,^{14}C)^{8}Be transfer reactions, from the raw files generated by the acquisition system, so we will cover from the calibration of the spectra required to visualize our data to the obtained angular distributions.

4.1 Calibration of the Spectra

To identify the scattered ^{13}C and the ^{12}C and ^{14}C produced particles of interest from the several elements that are also produced by the collision of ^{9}Be on ^{13}C, it is necessary to construct the two-dimensional identification spectrum, $\Delta E \times E_{total}$, where $E_{total}=\Delta E+E_{residual}$. Since we have to sum the signal from ΔE and $E_{residual}$, they both have to be calibrated. The ΔE signal is proportional to AZ^2/E. This comes from the approximation of

the Bethe-Bock equation, which determines the energy loss of charged particles passing through a material. So in the $\Delta E \times E_{total}$ plot, each element Z will appear as a hyperbole, with some separation in mass A, as shown in Figure 4.1. The region of the elements of interest for this work, $^{12,13,14}C$, is highlighted in the plot. The data obtained for the other elements, from different reactions, are being analyzed by other members of the group.

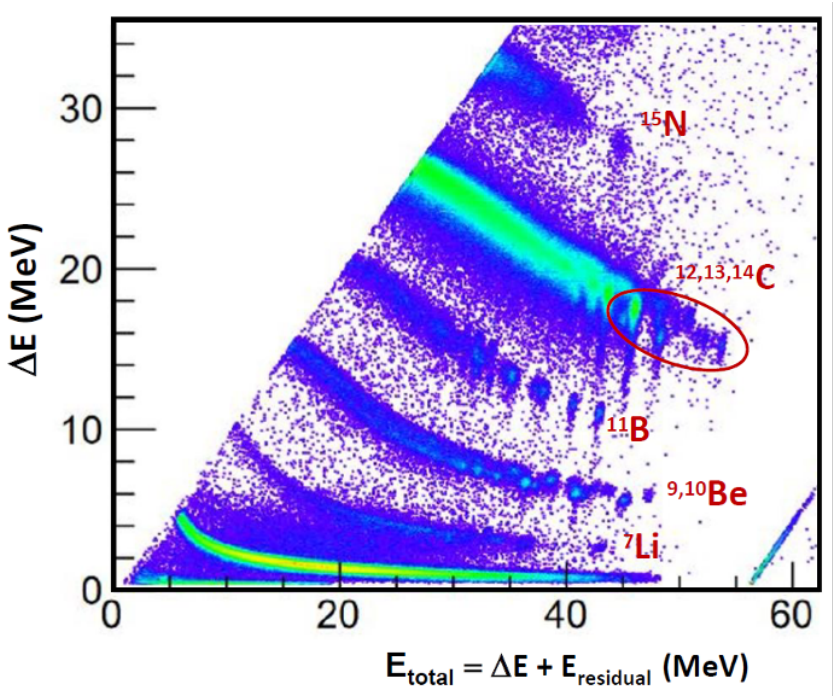

Figure 4.1: Calibrated $\Delta E \times E_{total}$ measured at θ_{Lab}=12.0^o E_{Lab}=55.0 MeV. Each of the bands represents one element with specific Z that was populated by the reactions induced in the collision of $^{13}C+^{9}Be$. The red circle indicates the region of interest of $^{12,13,14}C$.

As mentioned, to generate the $\Delta E \times E_{Total}$ spectrum, figure 4.1, the detectors had to be calibrated in energy. The calibration aims to establish a linear relation between the channels recorded by the acquisition system and the real energy at which the nuclei were produced. For this purpose, we measured the elastic scattering of ^{13}C on ^{197}Au. The target was placed at 20° relative to the beam direction, and the set of telescopes at 15°, 25°, 35° and 45°. The ^{13}C beam took on the energies of E_{Lab} = 30, 40, 50 and 55 MeV. At these energies and angles the scattering is Rutherford, but the important is that we can estimate the energy of the particles and establish the relation between energy and channel position of the particles in the spectra. A linear relation was obtained by identifying the centroid's position of the $^{13}C+^{197}Au$ elastic scattering peaks in channels and determining their corresponding energies. These energies were derived by performing kinematic calcu-

lation, considering energy loss in the target and detectors of the telescopes, each telescope consisting of a setup of two aligned silicon detectors: ΔE as the thin detector with a thickness of $22\mu m$, and E, as a thick detector with a thickness of $1000\mu m$. This calculations were performed using LISE++ platform (Tarasov and Bazin, 2008).

The calibration curves (linear relations) were defined by associating the centroid projections corresponding to ΔE onto the x-axis, representing the energy deposited into the thin detector, and the centroid projections corresponding to E onto the y-axis that represents the energy deposited into the thick detector. Once these deposited energy values were simulated in LISE++, we determined the parameters a and b of the linear calibration curves, related by the equation: $Energy = a * channel + b$. The obtained values of a and b used to calibrate each of the detectors are shown in Table 4.1.

Table 4.1 - Parameters of the Calibration Curves for each of the detectors used.

Detector	a	b
$E1$	0.0160	0.4314
$E2$	0.0162	0.2227
$E3$	0.0157	0.9340
$E4$	0.0163	0.0449
$\Delta E1$	0.0116	0.6338
$\Delta E2$	0.0119	0.2918
$\Delta E3$	0.0110	0.4679
$\Delta E4$	0.0127	-0.9648

4.2 Experimental differential cross sections

To calculate the experimental cross section for each angle and each process, what is needed is the relation of the incident flux with the outgoing flux, and the number of particles in the target. Equation 4.1 shows this relation. The differential cross section for a specific angle in the center of mass frame (θ_{cm}) is given by the number of particles scattered (or produced) in the detector (N^{det}_{counts}), within a certain solid angle (Ω_{det}) divided by the product of the number of incident particles (N_{beam}) and the number of particles in the target (N_{target}) as follows:

$$\frac{d\sigma}{d\Omega}(\theta_{cm}) = \frac{N^{\rm det}_{\rm counts}\, J\,(\theta_{cm}/\theta_{lab}) \times 10^{27}}{N_{\rm beam}\, N_{\rm target}\, \Delta\Omega_{\rm det}}(mb) \tag{4.1}$$

here the $J(\theta_{cm}/(\theta_{Lab})$ is the Jacobian converting from laboratory to center-of-mass system. The factor 10^{27} gives the differential cross section in units of milibarn.

To calculate the differential cross section for each measured angle, it is needed to find out the value of each of the terms in equation 4.1. These values are taken from the experimental setup, such as the geometrical characteristics of the target, the intensity of the beam, the position of the telescopes, and so on.

Peak integration (area) (N^{det}_{counts})

The information stored in the spectra is the number of events registered for each reaction collected by the telescopes at each measured angle. To find out the number of events, we have to identify and isolated the area of the peaks in the energy spectra corresponding to the scattering ^{13}C and reaction products ^{12}C and ^{14}C.

First, we have to identify these particles in the two dimensional ΔE$\times$E$_{total}$ spectra. As was stated in the previous section, the position of each particle in ΔE is proportional to AZ^2/E. This relation helps us to locate ^{12,13,14}C in the carbon band, taking into account their dependence on the atomic mass A, so it is expected to find ^{12}C lower than the intense ^{13}C scattered particles and ^{14}C at higher position.

In Figure 4.2, we show a zoom of the spectrum region with a clear identification of the band belonging to the carbon isotopes. Using the LISE++ package, we calculated the particle expected energy of the ^{13}C, ^{12}C$_{gs}$ and ^{13}C$_{gs}$ to accurately identify the peaks in the two-dimensional ΔE$\times$E$_{total}$ spectrum. Additionally, besides the peaks of interest, we also used other peaks, such as ^{9}Be$_{gs}$, ^{10}Be$_{gs}$ and ^{11}B$_{gs}$, to corroborate whether the calibration and peak identification was accurate. The values simulated with LISE++ package and obtained from the calibrated spectrum are listed in the table 4.2.

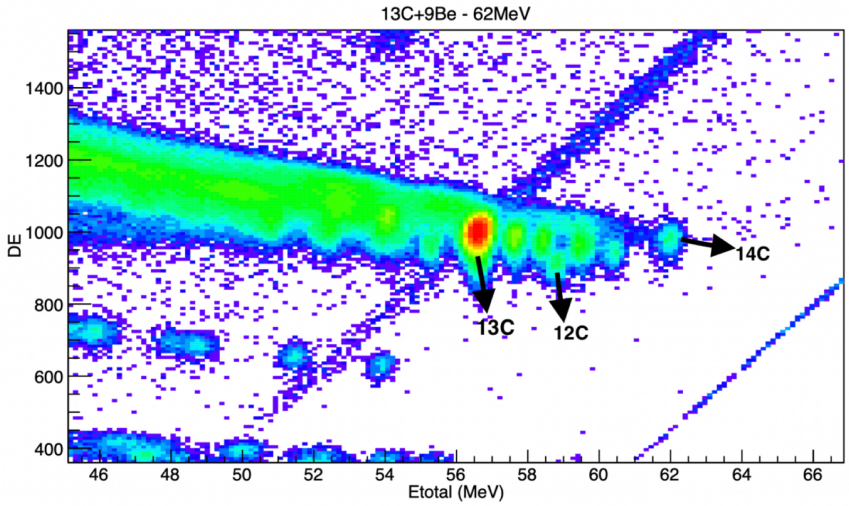

Figure 4.2: $\Delta E \times E_{total}$ spectrum for the reaction $^{9}Be(^{13}C,X)$ at E_{Lab}=62 MeV and θ_{Lab}=12.5°.

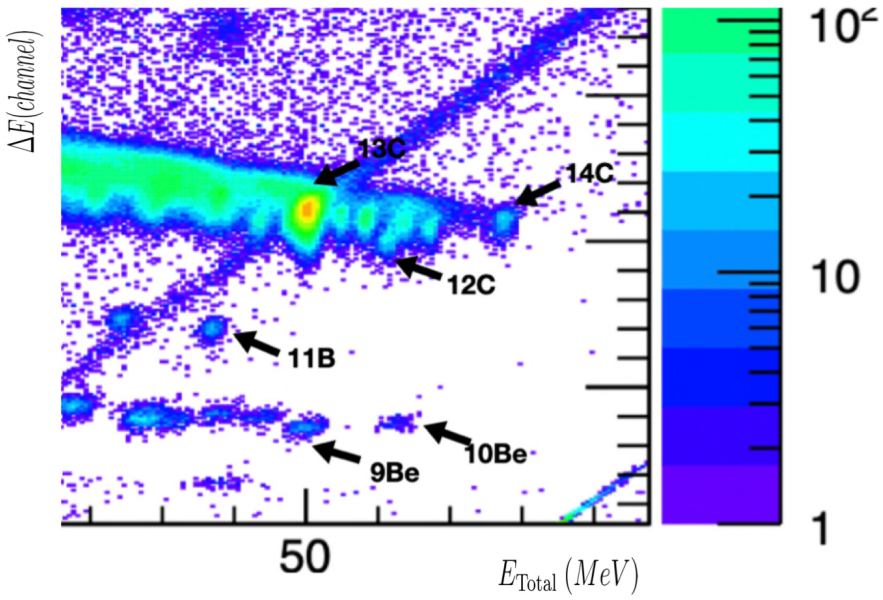

Figure 4.3: $\Delta E \times E_{total}$ highlighting the area with the peaks in the spectrum to verify the calibration for the $^{9}Be(^{13}C,X)$ reaction at E_{Lab} = 55 MeV and θ_{Lab} = 12.5°.

Table 4.2 - Calibration values and LISE++ simulations

Ions	Calibration (MeV)	LISE++ (MeV)
$^{12}C_{gs}$	52.27 ± 0.5	52.36
^{13}C	50.05 ± 0.5	52.10
$^{14}C_{gs}$	55.50 ± 0.5	55.64

Table 4.2 - Calibration values and LISE++ simulations

Ions	Calibration (MeV)	LISE++ (MeV)
$^{11}B_{gs}$	47.38 ± 0.5	47.26
$^{10}Be_{gs}$	52.54 ± 0.5	52.49
$^{9}Be_{gs}$	49.98 ± 0.5	48.89

Once the calibration was confirmed to be appropriate and the peaks were identified, each peak was located in all spectra and angles. To get the number of the corresponding particles, an integration procedure was adopted. The information stored in the spectra is the number of events for each reaction collected by the telescopes at each measured angle. To obtain the number of events of interest, we isolated the region in the spectrum (using a banana gate) where the peaks of ^{13}C, $^{12}C_{gs}$ and $^{14}C_{gs}$ were located, as shown in Figure 4.4 (B). We can projected this region in the x-axis, which corresponds to the total energy E_{Total}. This projection is shown in Figure 4.4 (C). As can be seen there as several other much smaller peaks corresponding to the elastic scattering of ^{13}C in the target contamination (^{12}C, ^{16}O, ^{28}Si and ^{58}Ni. The spectrum is in log scale and the contamination are really small. To get the area (or the counts) for the ^{13}C peak, we considered uniformity Gaussian fit setting a suitable background. This method was used to determine the counts of the elastic events, as well as for the $^{12}C_{gs}$ and $^{14}C_{gs}$ peaks.

Another important factor, which has to be taken into account to get the final number of events, is the deadtime, given by the Equation 4.2. The deadtime corresponds to the time the acquisition system is busy dealing with the previous event. To estimate this time, we recorded the counts of a pulser with a fix frequency of $f = 10Hz$ during the acquisition. In all spectra there was a peak at a fix position corresponding to the counts from the pulser. By using these counts, related to the reference frequency, we can estimate the deadtime for each run. In our case the deadtime was always around 1%, and it can be consider negligible.

$$deadtime = \frac{t_{\text{acquisition}} f}{N_{\text{counts}}^{\text{Pulser}}} \tag{4.2}$$

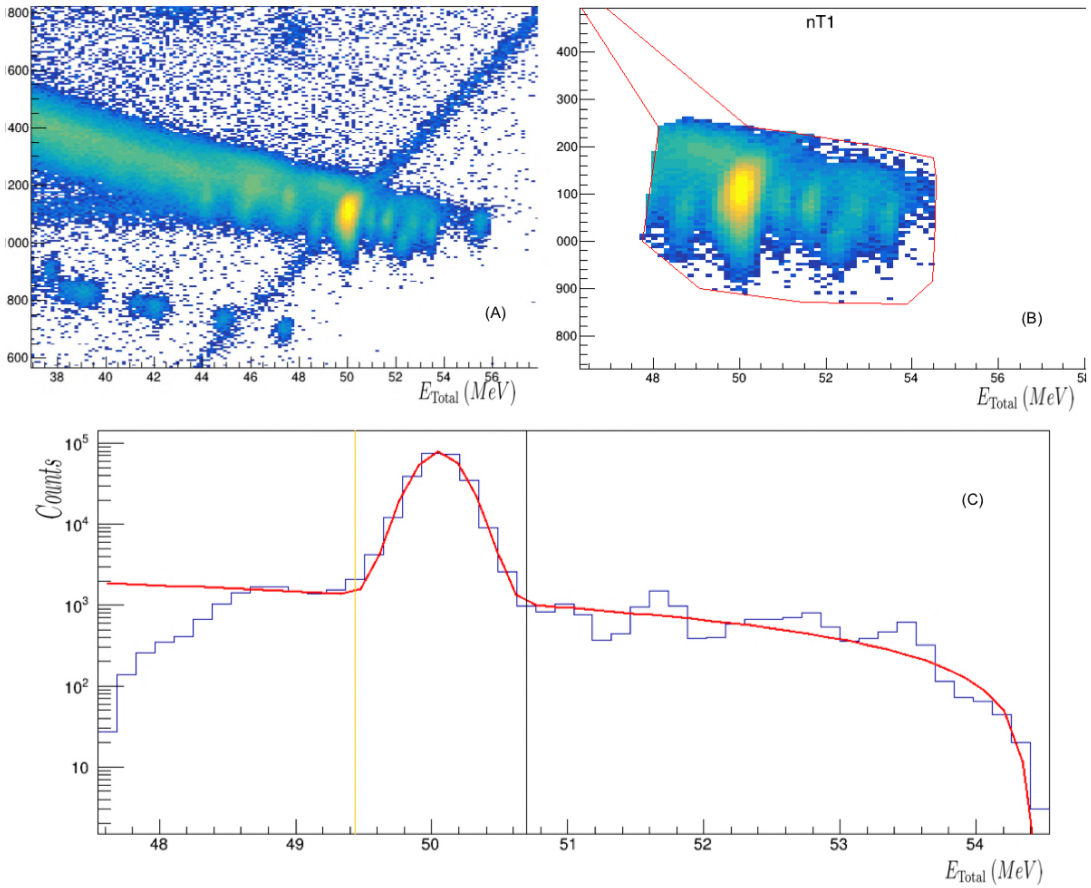

Figure 4.4: Spectrum of $^{9}Be(^{13}C, X)$ at $E_{Lab} = 55MeV$ and $\theta_{Lab} = 12.5°$ focusing attention on the Carbon band (A), (B) shows the area used to find out the counts in ^{13}C peak and to set the background and (C) Gaussian fitting to delimit the region considered to contain all the ^{13}C counts, the scale was logarithmic to show the linear background.

The counts of each peak are defined as the total counts, subtracting the background 4.3.

$$N_{counts} = N_{Total} - N_{Background} \tag{4.3}$$

Their uncertainty, given by statistical errors, is calculated as follows:

$$\delta N_{counts} = \sqrt{\delta N^2_{Total} + \delta N^2_{Background}} \tag{4.4}$$

Jacobian transformation of coordinates ($J(\theta_{cm}/\theta_{Lab})$)

To later compare the experimental angular distributions with the calculations, we have to express the differential cross section in the center of the mass frame. To convert it from the laboratory frame to center of mass, we have to apply a factor called Jacobian given by equation 4.5 (Arazi and Abriola, 2023).

$$J(\theta_{cm}/\theta_{Lab}) = \frac{d\left(\cos\theta_{Lab}\right)}{d\left(\cos\theta_{cm}\right)} = \frac{\left(1-\tau_b^2\sin^2\theta_{Lab}\right)^{1/2}}{\left(\tau_b\cos\theta_{Lab}+\left(1-\tau_b^2\sin^2\theta_{Lab}\right)^{1/2}\right]^2} \tag{4.5}$$

being

$$\tau_b = \left(\frac{m_a m_b}{m_A m_B}\frac{m_b+m_B}{m_a+m_A}\frac{E_{cm}}{E_{cm}+Q}\right)^{1/2} \tag{4.6}$$

where Q is the Q-value of the reaction, given by the mass differences, and $Q = 0$ for the elastic scattering.

$$Q = \left(m_a + m_A - m_b - m_B\right)c^2 \tag{4.7}$$

And E_{cm} stands for the energy of the ^{13}C beam in the center of mass frame:

$$E_{cm} = E_a\left(\frac{M_a}{M_a+M_A}\right) \tag{4.8}$$

Number of particles in the beam N_{beam}

During the irradiation, the beam intensity was monitored by a Faraday cup. The Faraday cup gives the current of the beam information, which can be integrated in time over the irradiation time to give the total charge integrated in terms of pulses. After the appropriate conversion we can get the total electric charge integrated, and knowing the charge state (q) of each beam particle, we can get the number of the incident particles using the expression 4.9:

$$N_{\text{beam}} = \frac{(\kappa)(n_p)}{e\bar{q}} \tag{4.9}$$

For the specific case of the TANDAR accelerator, we have $\kappa = 10^{-10} C/pulse$ and for the ^{13}C beam the average charge states were $\bar{q}$(55 MeV)= 5.97 and $\bar{q}$(62 MeV)= 5.99. The number of pulses is given by n_p and e is the charge of the electron.

Number of particles in the target (N_{target})

The target consisted of a pure ^{9}Be thin foil, 2μm thick, with a quite small amount of contamination. The number of particles in the target can be estimated by the relation with the molar mass:

$$N_{\text{target}} = \frac{\Delta x N_{\text{A}}}{A_{\text{target}} \cos(\alpha)} \tag{4.10}$$

In equation 4.10, Δx = 2.0 μm is the target thickness, N_A is the Avogadro's constant, A_{target}=9 is ^{9}Be atomic mass and α the angle at which the target was rotated in reference to the beam direction, for this experiment was 20°.

Solid Angle ($\Delta\Omega_{det}$)

At last, the detector's solid angles were estimated.

We calculate the solid angles by considering the geometry of the telescopes, specifically the area of the slit placed in front of each telescope as shown in Figure 4.5, and their distance to the target, listed in Table 4.3, with the Equation 4.11 (Arazi and Abriola, 2023). These dimensions were provided by the TANDAR staff and with them, we calculated the geometric solid angle 4.4 that was used to determine our angular distributions.

$$\Delta\Omega_{\text{Geo}}^{\text{det}} = \frac{A}{d^2} \tag{4.11}$$

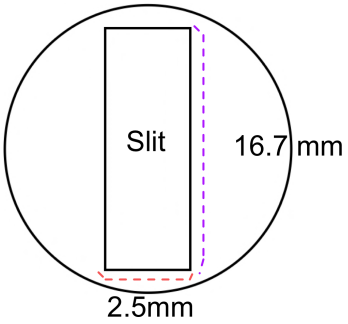

Figure 4.5: Illustration of the slit placed in front of the telescopes along with its dimensions

Table 4.3 - Distances from the target to the telescope

Detector	Distance (mm)
T_1	303
T_2	305
T_3	307
T_4	305

Table 4.4 - Geometric values of the Solid Angles $\Delta\Omega_{Geo}$

Detector	$\Delta\Omega_{\text{Geo}}$ (mSr)
T_1	0.455 ± 0.004
T_2	0.449 ± 0.004
T_3	0.443 ± 0.004
T_4	0.449 ± 0.004

4.3 Angular Distributions

Once all the necessary parameters have defined, estimated and determined, we calculated the differential cross sections for the angular distribution of the ^{9}Be(^{13}C,^{13}C)^{9}Be elastic scattering, Figure 4.6, and the neutron transfer reactions ^{9}Be(^{13}C,^{14}C)^{8}Be and ^{9}Be(^{13}C,^{12}C)^{10}Be, Figures 4.7 and 4.8 respectively, for the two energies measured E_{Lab} =

55 and 62 MeV. In the following chapter, we describe the theoretical analysis of these angular distributions. The uncertainties in the cross sections were taken only as the statistical error and varied between 1 and 2% for the most forward angles and 5% for the more backward angles. Additionally, there are some other systematic uncertainties related to the solid angle determination that was not extracted from the experiment but from given geometrical measurements and the thickness of the target that was not experimentally measured, which correspond to another 10 to 15% to be added to the differential cross sections.

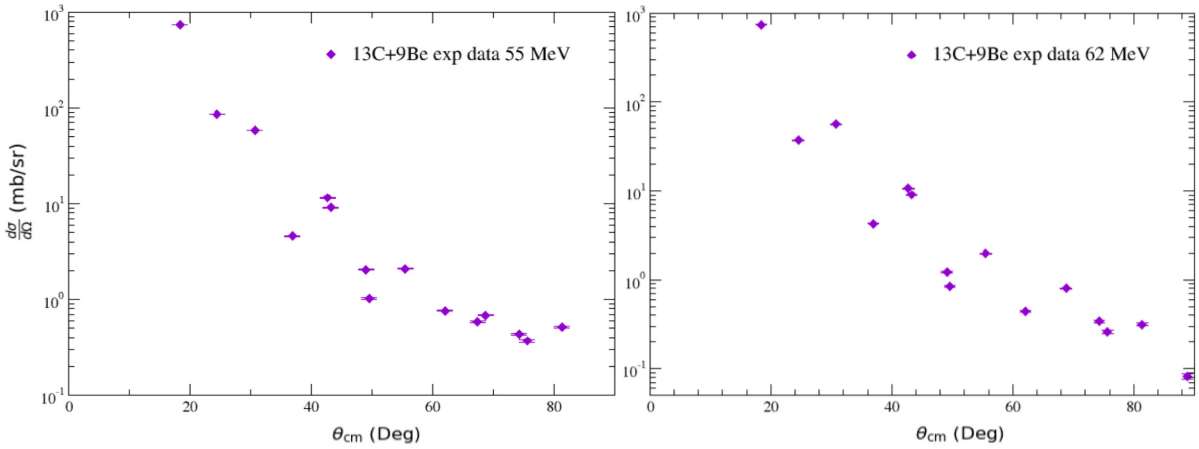

Figure 4.6: ^{9}Be(^{13}C,^{13}C)^{9}Be Experimental Angular Distributions at 55 MeV and 62 MeV energies

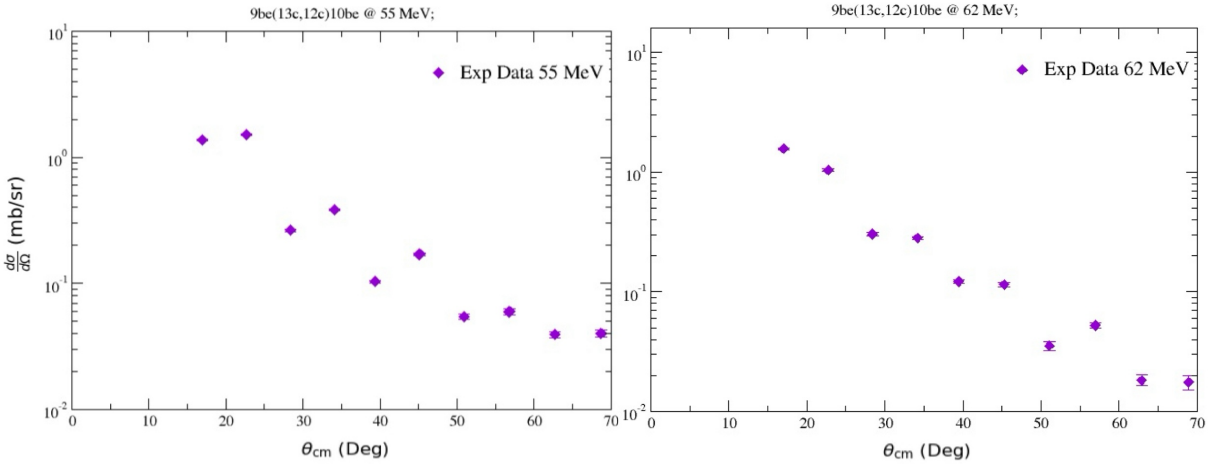

Figure 4.7: ^{9}Be(^{13}C,^{12}C)^{10}Be Experimental Angular Distributions at 55 MeV and 62 MeV energies

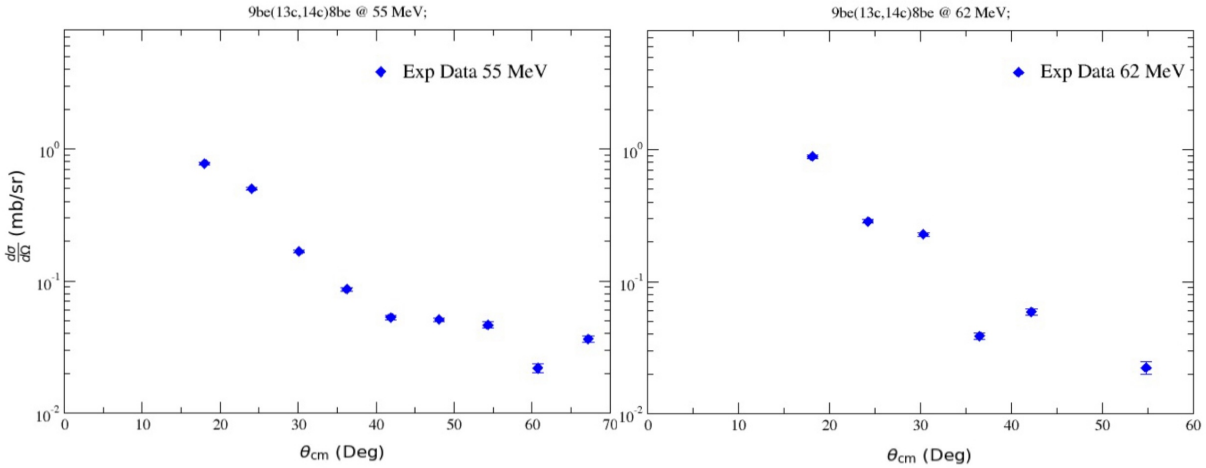

Figure 4.8: ^{9}Be(^{13}C,^{14}C)^{8}Be Experimental Angular Distributions at 55 MeV and 62 MeV energies

Chapter 5

Data Analysis

In this chapter we describe the theoretical analysis of the angular distributions obtained for both the elastic and neutron transfer reactions. All the calculations were performed using the code FRESCO (Thompson, 2006). Two distinct approaches were employed: the Optical Model for analysis of the elastic scattering and Distorted Wave Born Approximation (DWBA) calculations for the neutron transfers.

5.1 Optical model analysis for elastic scattering

The Optical Model is usually utilized to describe the elastic scattering between two colliding nuclei, where no internal structure is taken into account. To describe the angular distributions, a complex potential has to be considered, where the imaginary part is somehow responsible for the absorption of the elastic flux due various processes such as the fusion and other open channels, including inelastic scattering and direct reactions (transfer and breakup). In our analysis we initially considered potentials with Woods-Saxon shapes (Thompson and Nunes, 2009), which contains six parameters: real and imaginary depths (V_r and W), real and imaginary reduced radius (r_r and r_i) and real and imaginary difusiveness (a_r and a_i).

The potential employed in the optical model calculations should be complex as outlined by Thompson and Nunes (2009):

$$U = V(R) + iW(R) \tag{5.1}$$

Considering the Woods-Saxon shape for the potentials, we have:

$$V(R) = \frac{V_r}{1 + \exp\left(\frac{R-R_r}{a_r}\right)} \tag{5.2}$$

and

$$W(R) = \frac{V_i}{1 + \exp\left(\frac{R-R_i}{a_i}\right)} \tag{5.3}$$

We can either perform a fitting procedure, allowing some or all parameters free to vary, or get the set of the parameters from previous studies involving a system with similar mass and incident energy. In our case, the set of 6 parameters needed for the potential was taken from the literature. The first set, denoted as OM2, was extracted from the analysis of the elastic scattering of ^{9}Be+^{13}C, which was measured in direct kinematics (^{9}Be projectile on ^{13}C target) at E_{Lab}= 40.0 MeV by Li et al. (2013). The center of mass the energy, E_{cm}=23.63 MeV, is very similar to our energies, E_{cm}=22.5 and 25.4 MeV. The set referred as OM1 was derived from the study by Marzhan Nassurlla et al. (2021), where the authors used the same data as the previous one but employed a different set of parameters for the potential. These sets of parameters are listed in Table 5.2. In this context the radius of the nuclei is given by $R = r_0 \times (A_P^{1/3} + A_T^{1/3})$, where the reduced radius as either r_i or r_r. The results of the OM calculations for the angular distributions, measured at E_{Lab}=55.0 and 62.0 MeV, using these potentials, are shown in Figure 5.1. As evident from the figure, both potentials describe the elastic scattering angular distributions at forward angles quite well. At more backward angles, the description is not so good, likely due to influence of other channels that might be present, such as contributions from the alpha transfer ^{9}Be(^{13}C,^{9}Be)^{13}C, or other transfer reactions. These additional channels could potentially affect the angular distributions, particularly at large scattering angles. For completeness of the analysis, we also included the results obtained with the double-folding São Paulo Potential (Chamon et al., 2002), utilizing the standard normalization factors N_R=1.0 and $N_I = 0.78$. This potential, usually considered as benchmark, demonstrated good agreement with the experimental data for most forward angles but did not at backward angles. Again, this is a clear indication of the importance of other channels stealing flux from elastic. For the following analysis of the transfer reaction we are going to use the OM1 potential, since

it better described a wider range of the angular distributions. It is important to emphasize that no parameter adjustment has been done. These are strait calculations, using the mentioned parameters.

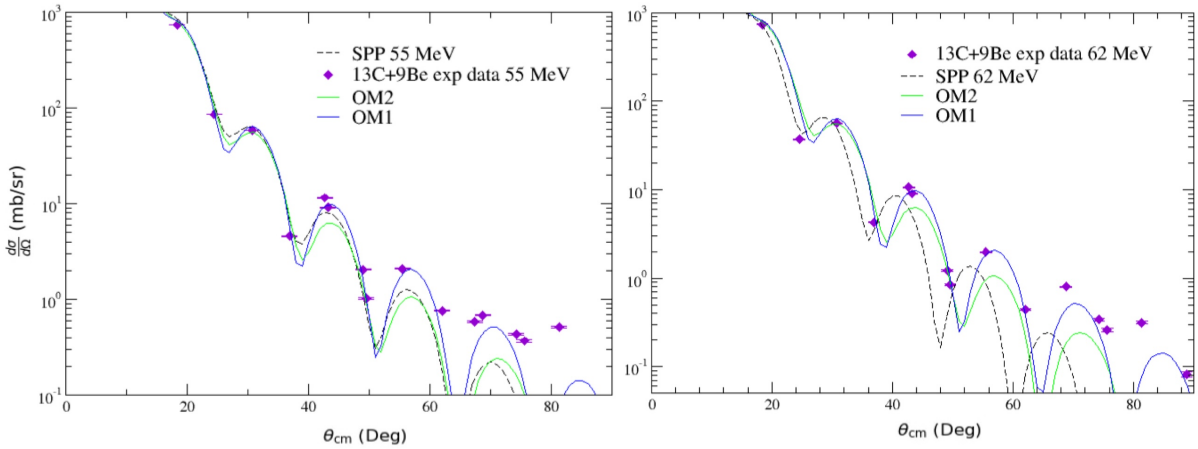

Figure 5.1: Experimental angular distribution ^{9}Be(^{13}C,^{13}C)^{9}Be, E$_{Lab}$=55.0 and 62.0 MeV with the calculation using the Optical Model with Woods-Saxon and Sao Paulo Potentials

Table 5.1 - Optical Model Parameters

Pot	V_r (MeV)	r_r (fm)	a_r (fm)	V_i (MeV)	r_i (fm)	a_i (fm)	r_c (fm)
$OM1$	175	0.8	0.788	25.2	1.25	0.522	1.25
$OM2$	127	0.8	0.78	13.9	1.25	0.7	1

5.2 Angular Distributions of the Neutron Transfer Reactions.

The main motivation of this analysis is to determine the spectroscopic factors for the $<^{12}$C+n$|^{13}$C$>$ and $<^{13}$C+n$|^{14}$C$>$ systems: SF$_{^{12}C+n}$ and SF$_{^{13}C+n}$ respectively. For this purpose, we are considering the neutron transfer reactions ^{9}Be(^{13}C,^{14}C)^{8}Be and ^{9}Be(^{13}C,^{12}C)^{10}Be. We employed the DWBA (Distorted Wave Born Approximation) calculations, using the FRESCO code (Thompson, 2006). The idea of this analysis is to perform the DWBA calculations under the appropriate conditions, potentials, spin, and angular momentum, to reproduce the oscillations observed in the angular distribution. The normalization of

the calculated angular distribution to the experimental one provides the product of the spectroscopic factors of the two vertices of the reaction, as shown in Equation 5.4. If the spectroscopic factor of one vertex is known, the other can be determined.

$$\left(\frac{d\sigma}{d\Omega}\right)_{\text{exp}} = S_1 S_2 \left(\frac{d\sigma}{d\Omega}\right)_{\text{DWBA}} \tag{5.4}$$

For the neutron transfer ^{9}Be(^{13}C,^{12}C)^{10}Be reaction, S_1 and S_2 should be replaced by $SF_{^{9}Be+n}$ and $SF_{^{12}C+n}$, respectively, while for the ^{9}Be(^{13}C,^{14}C)^{8}Be reaction they should be replaced by $SF_{^{8}Be+n}$ and $SF_{^{13}C+n}$, i.e.:

$$S_1 S_2 = SF_{^{9}Be+n} SF_{^{12}C+n} \tag{5.5}$$

and

$$S_1 S_2 = SF_{^{8}Be+n} SF_{^{13}C+n} \tag{5.6}$$

The results of the DWBA calculations for the angular distributions of the neutron transfer ^{9}Be(^{13}C,^{12}C)^{10}Be at both E_{Lab} = 55 MeV and 62 MeV are present in Figure 5.2. These angular distributions are already normalized.

The transfer reaction involves two partitions, the entrance, ^{9}Be+^{13}C, and exit, ^{10}Be+^{12}C channels. Also, there are two bound states: ^{10}Be=^{9}Be+n and ^{13}C=^{12}C+n. In the DWBA calculations, a potential must be defined for each of these systems. For the entrance channel, ^{9}Be+^{13}C, we used the Woods-Saxon potential OM1, obtained in the previous analysis (Marzhan Nassurlla et al., 2021). However, for the exit channel, ^{10}Be+^{12}C, there were no available elastic scattering measurement or analyses. Therefore, we considered the Woods-Saxon potential parameters from a similar system, ^{9}Be+^{12}C (Li et al., 2013), of course, taken into account the spin difference, $J^{\pi}(^{9}\text{Be}) = 3/2^{-}$ and $J^{\pi}(^{10}\text{Be}) = 0^{+}$. The authors from ref. Li et al. (2013) considered the extra spin-orbit potential to better describe the elastic scattering of ^{9}Be+^{12}C system. However, calculating with and without the spin-orbit term,

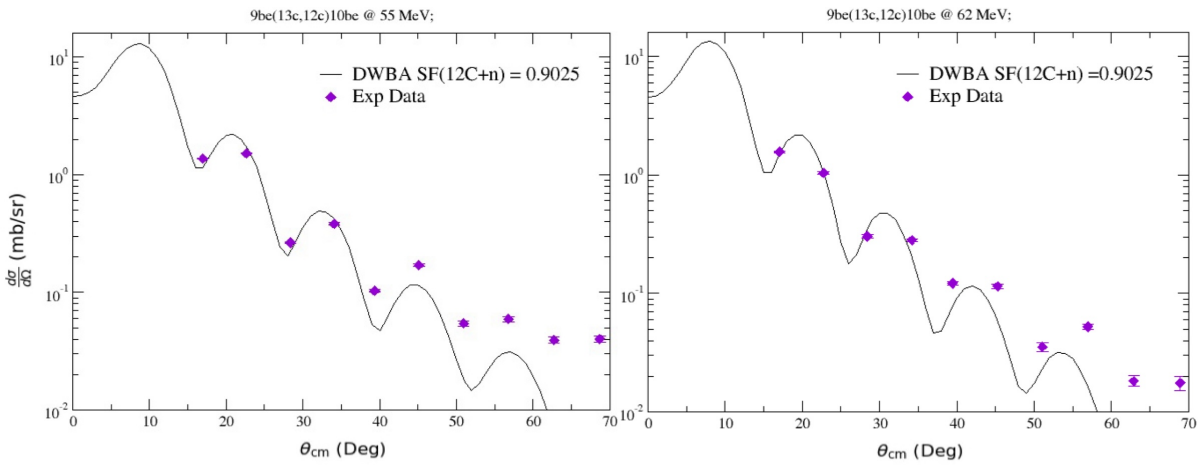

Figure 5.2: Angular distributions for the neutron transfer ^{9}Be(^{13}C,^{12}C)^{10}Be reaction at E_{Lab} = 55.0 and 62.0 MeV, along with the results of the DWBA calculations.

as shown in Figure 5.3, no difference was observed for our data. Hence, we neglected this spin-orbit term in our calculations. For the bound states we used a Woods-Saxon shape with the geometric standard parameters a=0.65 fm for the difusiveness and r=1.25 fm for reduced radius, respectively. The depth of the potential was automatically adjusted by the FRESCO code to the bound energy of the corresponding system.

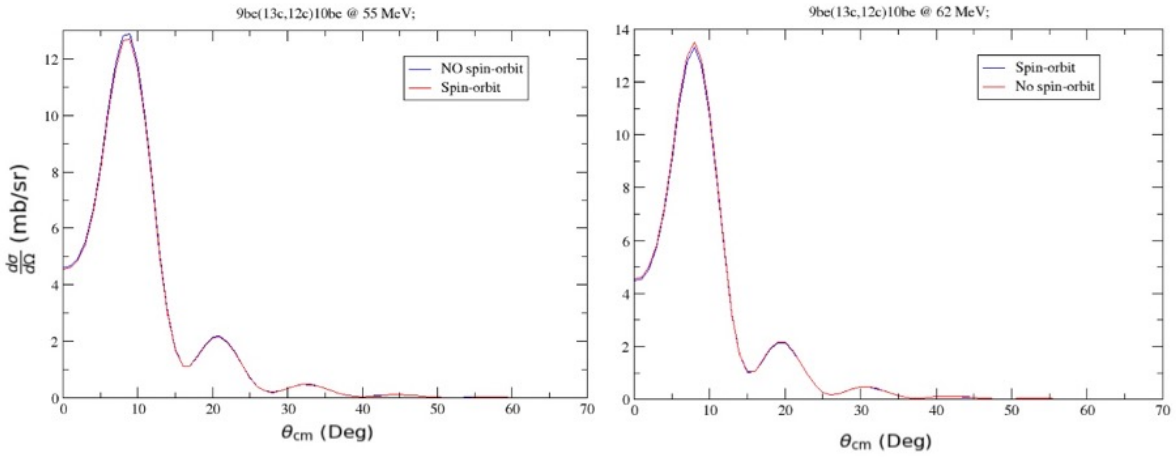

Figure 5.3: DWBA calculation with and without the spin-orbit term for the neutron transfer ^{9}Be(^{13}C,^{12}C)^{10}Be reaction.

Table 5.2 - Parameters for the potentials used in the DWBA calculations for the ^{9}Be(^{13}C,^{12}C)^{10}Be reaction

Channel	V_r (MeV)	r_r (fm)	a_r (fm)	V_i (MeV)	r_i (fm)	a_i (fm)	r_c (fm)
Entrance*	175	0.8	0.788	25.2	1.25	0.522	1.25
Exit**	33.69	0.97	0.92	6.52	1.51	0.48	1.20

*^{9}Be+^{13}C (Marzhan Nassurlla et al., 2021) **^{9}Be+^{12}C (Li et al., 2013)

Using the spectroscopic $SF_{^{9}Be+n} = 1.58 \pm 0.15$ from Ref. (Lee et al., 2007) we got the spectroscopic-factor $SF_{^{12}C+n} = 0.90 \pm 0.10$ for the $<^{12}$C+n$|^{13}$C$>$ system. This value is consistent with the one obtained from the average of several neutron stripping reaction, ^{13}C(p,d)^{12}C, $SF_{^{12}C+n} = 0.81 \pm 0.12$ from ref. (Lee et al., 2007). This result is an indication that the adopted procedure and the use of a heavier projectile for the transfer of a neutron, (^{9}Be,^{10}Be), is valid.

The same methodology was applied to calculate the spectroscopic factor of the system $<^{13}$C+n$|^{14}$C$>$ from the neutron transfer ^{9}Be(^{13}C,^{14}C)^{8}Be. For the entrance channel, we used the same OM1 Woods-Saxon potential as the elastic scattering ^{9}Be+^{13}C (Marzhan Nassurlla et al., 2021). The exit channel corresponds to elastic scattering ^{14}C+^{8}Be. This system cannot be measured since ^{8}Be is not bound. After extensive bibliographical research and testing, we found some analyses of the elastic scattering of ^{14}N+^{10}B Motobayashi et al. (1979). This system is quite similar to the ^{14}C+^{8}Be, and we adopted the same parameters, as listed in Table 5.3.

Figure 5.4 shows the result of the DWBA for the angular distribution for the neutron transfer ^{9}Be(^{13}C,^{14}C)^{8}Be, together with the experimental angular distribution already normalized. Utilizing the Equation 5.4 and replacing S_1 with $SF_{^{8}Be+n} = 0.45 \pm 0.03$, also obtained from an average of ^{9}Be(p,d)^{8}Be reaction (Lee et al., 2007), we derive the spectroscopic value of $SF_{^{13}C+n} = 1.21 \pm 0.12$ for the ^{14}C=^{13}C+n system at both energies. The ref. (Lee et al., 2007) indicates only two works using the pickup ^{13}C(d,p)^{14}C reaction, with spectroscopic values of SF=1.94 and 1.82. On the other hand, using the stripping ^{14}C(p,d)^{13}C reaction, the averaged values of the spectroscopic factors value is $SF_{^{13}C+n} = 1.50 \pm 0.30$, which is more consistent with the value obtained in the present

work.

The uncertainty of the spectroscopic factors $SF_{^{12}C+n}$ and $SF_{^{13}C+n}$ was determined propagating the uncertainties of the spectroscopic factors taken from the literature and the uncertainty presented in the experimental angular distributions, accounting for statistical error.

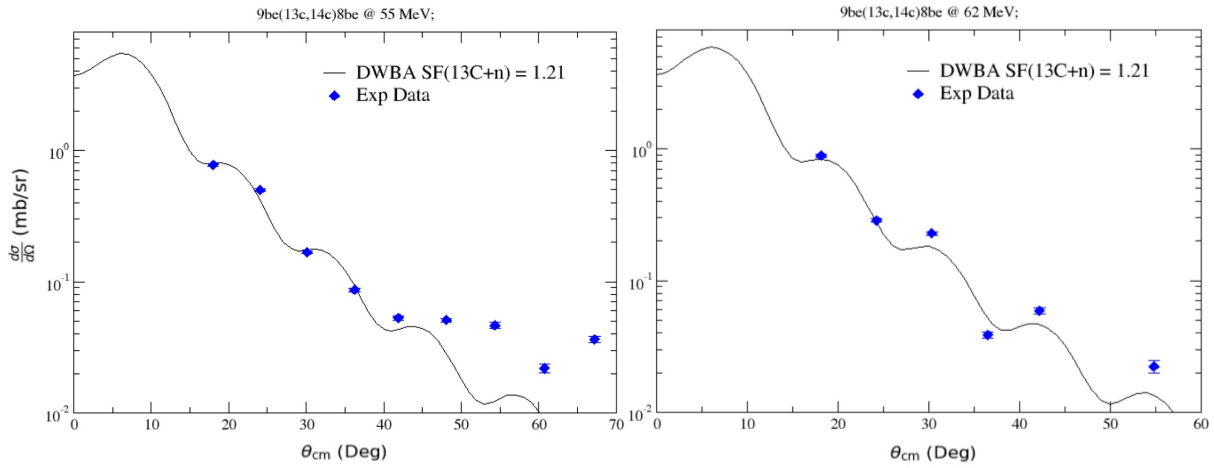

Figure 5.4: DWBA calculation performed using FRESCO code of the neutron transfer reaction $^{9}Be(^{13}C,^{14}C)^{8}Be$ to find out $S_{^{13}C+n}$ together with the experimental angular distribution calculated in chapter 4.

Table 5.3 - Potential parameters used in the analysis of the $^{9}Be(^{13}C,^{14}C)^{8}Be$ reaction.

Channel	V_r (MeV)	r_r (fm)	a_r (fm)	V_i (MeV)	r_i (fm)	a_i (fm)	r_c (fm)
Entrance*	175	0.8	0.788	25.2	1.25	0.522	1.25
Exit**	76	0.92	0.77	28	1.29	0.415	1

*$^{9}Be+^{13}C$ (Marzhan Nassurlla et al., 2021) ** $^{14}N+^{10}B$ (Motobayashi et al., 1979)

5.3 *Neutron Capture $^{13}C(n,\gamma)^{14}C$ and $^{12}C(n,\gamma)^{13}C$ reactions.*

Indeed, in astrophysical contexts, usually fusion reactions occur through the compound–nucleus formation, which involves a very large number of resonances. When one of the involved nuclei is a very light particle (such as neutron, proton, deuterium and alphas),

we refer it as a capture reaction, which can be direct radiative capture (DRC), with no resonances involved or resonant capture, when the capture passes through wide or narrow resonances, see Figure 5.5 for a schematic view. Even for direct capture cross section, calculations are are not simple and it might be necessary to solve a many-body problem for the bound and continuum states.

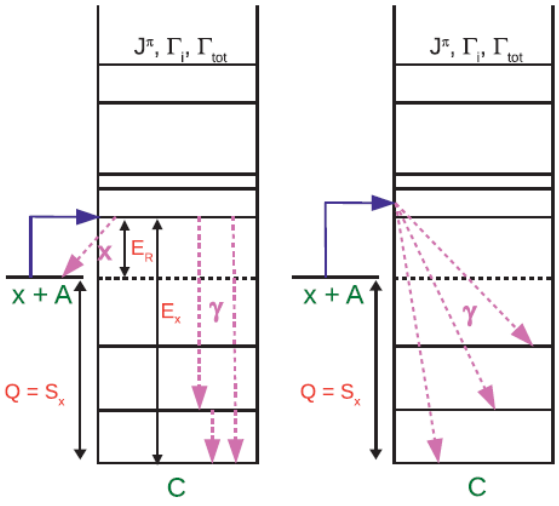

Figure 5.5: Schematic view of resonant (left) and direct (right) capture reaction

To overcome the difficulties related to the many-body, simpler calculations have been developed to calculate direct capture reactions based on approximations. One of them is based on a potential model, which relies on the use of potentials to obtain single-particle energies and wave functions. The potential model assumes two structureless particles interacting via a potential with a relative coordinate dependence determined by a set of adjustable parameters. With appropriate potentials and parameters this solution can be considered good enough to give cross sections, within the accuracy required to reproduce the experimental data. The potential model requires, then, good potentials to describe both the bound and continuum states, as well as an operator to connect them. The bound potential produces the bound state wave function, which should be then normalized by the spectroscopic factor. The wave functions for the continuum states can be produced by the scattering potential of the interacting nuclei. The operator which connects the bound and continuum wave functions depends on the transition type (E1, E2, M1, etc) and the angular momentum of the nuclei involved. A more detail of the potential model can be

found, for instance, in the ref. (Huang et al., 2010).

It is important to emphasize that the potential model calculates only the direct capture cross section, and it is given by:

$$\sigma_{L,J_c}^{DRC}(E) = | < \Psi_{scat}(r)||r^L Y_L||I_{bound}(r) > |^2 \tag{5.7}$$

where $I_{bound}(r)$ is the overlap integral related to the bound state, J_c is the spin of the composite system ($C = A + n$), $\Psi_{scat}(r)$ is the scattering wave function for the $A + n$ system and $r^L Y_L$ is the multipolarity transition operator (EL, ML). As an example, the direct radiative capture (DRC) of an s-wave and/or d-wave nucleon (proton or neutron) by a nucleus A, proceeding via $E1$ transition, leaving the compound nucleus C in its ground state, is given by:

$$\sigma_{A\to C}^{E1}(E) = \frac{16\pi}{9\hbar}\kappa_\gamma^3 | < \Psi_{scat}||O^{E1}||I_{bound}(r) > |^2 \tag{5.8}$$

where κ_γ^3 is the wave number corresponding to a γ-ray with energy ϵ_γ, O^{E1} stands for the electric dipole operator.

In the potential model, to calculate the overlap function, we have to know the wave function of the bound state and the spectroscopic fator: $I_{bound}(r) = SF_{J_c} \times \Psi_{bound}$, where this wave function can be calculated using the bound potentials if standard parameters as r=1.25 fm and a=0.65 fm.

The total direct capture cross section is obtained by adding all multipolarities and final spins of the bound state is given by:

$$\sigma^{DRC}(E) = \sum_{L,J_c} SF_{J_c}\sigma_{LJ_c}^{DRC}(E) \tag{5.9}$$

here SF_{J_c} is the spectroscopic factor for the final bound state with spin J_c.

The imprints of many-body effects eventually disappear at large distances between the nucleon and the nucleus, and the overlap function, $I_{bound}(r)$, asymptotically matches with the solution of the Schrödinger equation with $V = V_C$ (pure Coulomb) for protons

and and $V = 0$ (pure nuclear potential) for neutron (r $\rightarrow \infty$). We can, thus, consider this approximation to calculate capture reactions under the assumption that the capture is peripheral. This approximation is then called Asymptotic Normalization Coefficient (ANC) and:

$$I_{bound}(r) = ANC\frac{W_{-\eta,l_{b+1/2}}(2\kappa r)}{r} \text{ for protons} \tag{5.10}$$

and

$$I_{bound}(r) = ANC\sqrt{\frac{2\kappa}{r}}K_{-\eta,l_{b+1/2}} \text{ for neutrons} \tag{5.11}$$

where the binding energy of the $C = A+x$ system is related to κ by means of $E = \hbar^2\kappa^2/2m$, $W_{\eta,l_{b+1/2}}$ is the Whittaker function and $K_{-\eta,l_{b+1/2}}$ is the modified Bessel function.

When the capture reaction is peripheral, the solution and the particle capture occurs at a certain distance from the nucleus, only the asymptotic part of the bound-state wave function contributes to the determination of the capture cross section. And as mentioned, asymptotically, the bound state wave function, $I_{bound}(r)$, for the system $C = a + x$ can be determined by the known Whittaker and modified Bessel functions, for protons and neutrons, respectively. The normalization, however, should be provided by the coefficient ANC. As the overlap integral asymptotically becomes a Whittaker function, so does the single particle bound-state wavefunction Ψ_{bound}. The relation between the ANC obtained from experiment or a microscopic model, with the single particle ANC, is given by:

$$(ANC_i)^2 = SF_i(b_i)^2 \tag{5.12}$$

here b_i is the single particle ANC.

The values of SF_i and b_i can be obtained from a simple potential model and are related to the complex short-range many-body physics of radiative capture reactions. These parameters are strongly dependent on the parameters and model of the chosen potential. On the other hand, these effects are canceled by taking their products. The ANC coefficient are then influenced only by the asymptotic behavior of the bound-wave function and do not depend on the choice of the potential used to obtain the wave-function.

5.3.1 $^{9}Be(^{13}C,^{14}C)^{8}Be$ and $^{9}Be(^{13}C,^{12}C)^{10}Be$ Peripheral Nature

We checked the peripherality of the neutron transfer reactions ^{9}Be(^{13}C,^{12}C)^{10}Be and ^{9}Be(^{13}C,^{14}C)^{8}Be reactions, we performed the DWBA calculations cutting the internal radius of integration. In Figure 5.6, we show the results of changing the lower radius limit of the integration. The grazing radius for the ^{13}C+^{9}Be system (when the two colliding nuclei are just touching each other) is given by $R_{grazing} = r_0(A_A^{1/3} + A_a^{1/3}) = 5.5fm$ with $r_0 = 1.25fm$. As observed in the figure, the cross-sections do not change much for $radii < 6$ fm, especially in the forward angles region where the transfer is dominant. This indicates that, indeed, the internal part of the nuclear potential does not imply a significant influence, and we can conclude that both neutron transfer reactions are peripheral.

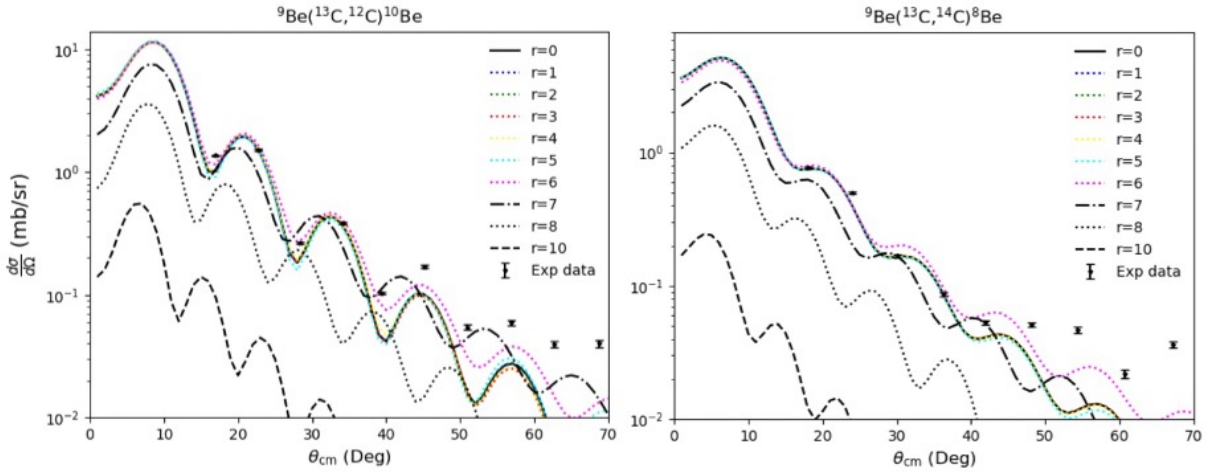

Figure 5.6: $^{9}Be(^{13}C,^{14}C)^{8}Be$ and $^{9}Be(^{13}C,^{12}C)^{10}Be$ Peripheral Test

5.3.2 $^{13}C(n,\gamma)^{14}C$ and $^{12}C(n,\gamma)^{13}C$ Neutron Capture Calculation

In section 5.2 we described how we determined the spectroscopic factors $SF_{^{12}C+n}$ and $SF_{^{13}C+n}$. Now, we can use these spectroscopic factors, associated with the potential model, to calculate the neutron capture reactions. For this purpose, we utilized the RADCAP code (Bertulani, 2003). We calculated the cross-section of the direct neutron capture reactions ^{12}C(n,γ)^{13}C$_{gs}$ and ^{13}C(n,γ)^{14}C$_{gs}$ to the ground state using the spectroscopic factors determined in chapter 4, $SF_{^{12}C+n} = 0.90 \pm 0.10$ and $SF_{^{13}C+n} = 1.21 \pm 0.12$, respectively.

Besides the spectroscopic factors, for the input file of RADCAP, we also need the parameters of the potential corresponding to the neutron capture to the ground state. We

used the values obtained in Ref. Mengoni et al. (1995), except for the value of the potential depth, which was adopted from Ref. Huang et al. (2010) as this value was not available in Mengoni et al. (1995). Those values are listed in Table 5.4. The depth for transition to the ground state for the ^{13}C(n,γ)^{14}C reaction was set as $V_0^{^{13}C+n} = -15.02$ MeV. This value was obtained by keeping the same volume integral as for the ^{12}C(n,γ)^{13}C reaction.

To calculate the capture cross section for both the ^{12}C(n,γ)^{13}C and ^{13}C(n,γ)^{14}C reactions, we also had to consider that the capture proceeded by s and d waves, as well as by $E1$ capture. The spins (in the ground states) of the involved nuclei were also included in the input file: ^{12}C ($J^\pi = 0^+$), ^{13}C ($J^\pi = 1/2^-$), ^{14}C ($J^\pi = 0^+$), n ($J^\pi = 1/2^+$), with the relative angular momentum, l=1. For the bound state the geometrical factors r=1.25 fm and a=0.65 fm were adopted, with the corresponding depth adjusted to reproduce the binding energy, $B_{^{12}C+n}$=4.946 MeV and $B^{13}C + n$=8.176 MeV. The complete input for the code is in the appendix.

Table 5.4 - RADCAP parameters used to calculate ^{12}C(n,γ)^{13}C and ^{13}C(n,γ)^{14}C capture reactions.

- System	V_0 (MeV)	r_0 (fm)	a_A (fm)	V_{S0} (MeV)	r_{S0} (fm)	a_{AS} (fm)	r_C (fm)
^{12}C+n	-14.75	2.86	0.62	-7.00	2.86	0.62	2.86
^{13}C+n	-15.02	2.94	0.62	-7.00	2.94	0.62	2.94

The potential is a Woods-Saxon potential with:

- V_0, depth of the central potential
- r_0, radius of the central potential
- a_A, diffuseness of the central potential
- V_{S0}, depth of the spin-orbit potential
- r_{S0}, radius of the spin-orbit potential
- a_{AS}, diffuseness of the spin-orbit potential

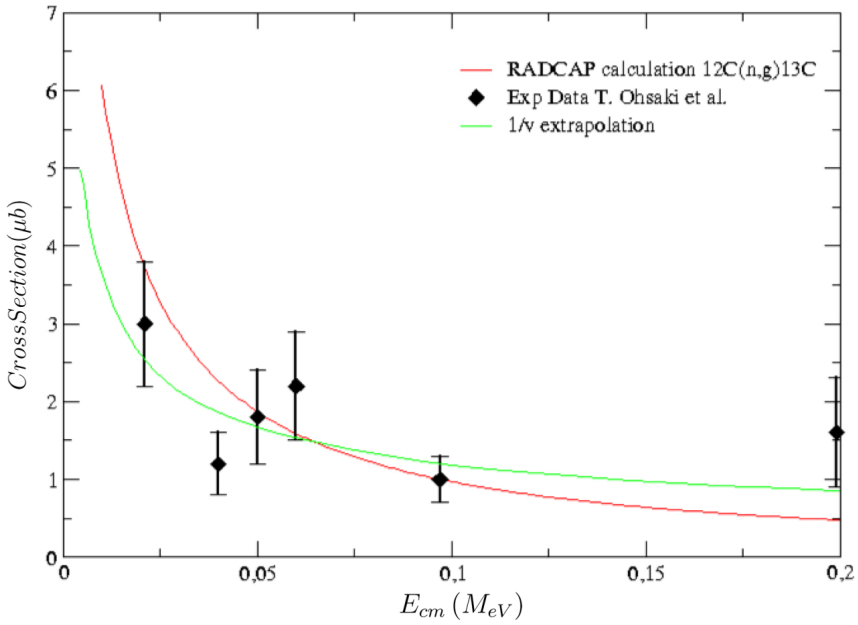

Figure 5.7: Cross Section of the ^{12}C(n,γ)^{13}C Direct Neutron Capture Reaction calculated with RADCAP, compared with the experimental data taken from Ohsaki et al. (1994)

- r_C, Coulomb radius

In Figure 5.7, we plot the results of the theoretical calculation, using RADCAP code, together with the experimental data acquired by Ohsaki et al. (1994). As one can see, the calculation reproduced the data, although the uncertainty is significant. Reliability of the present method to calculate the cross section has been demonstrated previously and has shown good agreement for several other systems in ref. Huang et al. (2010).

For the ^{13}C(n,γ)^{14}C reaction, there is data only below 100 keV. At this energy, the cross sections is dominated by a strong p-wave resonance at E_n = 143 keV and by the non-resonant s-wave direct capture to the ground state. In our study we estimated the contribution of the non-resonant, direct capture reaction, shown in Figure 5.8. The resulting curve agrees well with the previous work at the thermal energy region (Herndl et al., 1999). Moreover, for both reactions, although very similar, the calculated curves do not follow exactly the $1/v$ trend for the thermal energy.

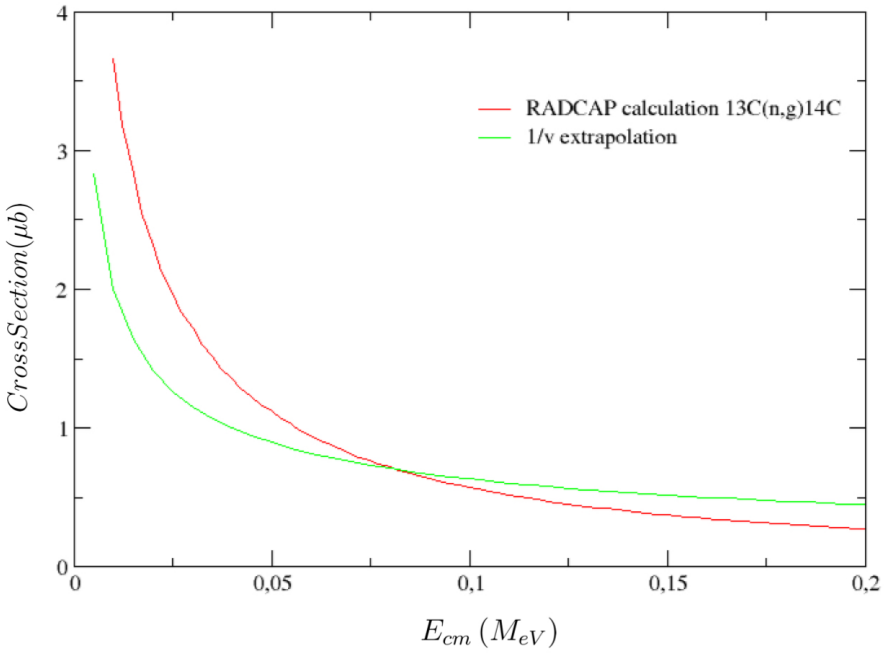

Figure 5.8: Cross Section of the $^{13}C(n,\gamma)^{14}C$ Direct Neutron Capture Reaction calculated with RADCAP

Chapter 6

Conclusions

The goal of this work was to obtain the spectroscopic factors for the $<^{12}$C+n$|^{13}$C$>$ and $<^{13}$C+n$|^{14}$C$>$ systems: $SF_{^{12}C+n}$ and $SF_{^{13}C+n}$, respectively, and to calculate the neutron capture cross-sections for the ^{12}C(n,γ)^{13}C and ^{13}C(n,γ)^{14}C reactions. For this purpose, an experiment was conducted at the TANDAR accelerator located in Buenos Aires, Argentina. In this experiment we bombarding the ^{13}C beam at E_{Lab}=55.0 and 62.0 MeV on a thin foil pure ^{9}Be target. From the collision of these nuclei, we measured angular distributions for the elastic scattering and neutron transfer ^{9}Be(^{13}C,^{14}C)^{8}Be and ^{9}Be(^{13}C,^{12}C)^{10}Be reactions at these two energies.

The elastic scattering angular distributions obtained in the experiment were analyzed with Optical Model using Woods-Saxon potentials. These angular distributions were well described by the Optical Model (OM) with the potentials considered. This allowed us to get good potentials for the scattered particles, which could be later, used in the analysis of the transfer reactions. The angular distributions for the transfer reactions were analyzed with DWBA calculations, where the previous potentials were used to obtain the distorted waves. By comparing the calculated angular distributions with the data we can obtain the product of the spectroscopic factors of the two vertices of the reaction. Once the spectroscopic of one vertex is known the other can be determined. In the present work, using the known spectroscopic $SF_{^{9}Be+n} = 1.58 \pm 0.15$ from Ref. (Lee et al., 2007), we obtained the spectroscopic factor $SF_{^{12}C+n} = 0.90 \pm 0.10$ for the $<^{12}$C+n$|^{13}$C$>$ system, which is consistent with the value from previous (p,d) reactions. For the $<^{13}$C+n$|^{14}$C$>$ system, the spectroscopic factor was obtained from the neutron transfer ^{9}Be(^{13}C,^{14}C)^{8}Be. Using the known $SF_{^{8}Be+n} = 0.45 \pm 0.03$, from an average of ^{9}Be(p,d)^{8}Be reaction (Lee et al., 2007), we obtained the spectroscopic value of $SF_{^{13}C+n} = 1.21 \pm 0.12$ for the ^{14}C=^{13}C+n

system for both energies E_{Lab} = 55 and 62 MeV. This value is consistent with the one obtained from ^{14}C(p,d)^{13}C reaction ($SF_{^{13}C+n} = 1.50 \pm 0.30$).

With the obtained spectroscopic factors, we can estimate the direct radiative neutron capture using the Potential Model. This model is an approximation in which the colliding nuclei are described by structureless particles, and in which the scattering and bound wave function can be determined by specific potentials. This model is particularly useful to estimate direct neutron capture cross sections for radioactive elements, since a direct measurement would not be, experimentally, possible. We use the obtained spectroscopic factors for the $<^{12}$C+n$|^{13}$C> and $<^{13}$C+n$|^{14}$C> systems to infer about the direct component of the ^{12}C(n,γ)^{13}C and ^{13}C(n,γ)^{14}C neutron capture reactions. Our results for the ^{12}C(n,γ)^{13}C reaction reproduced the available data; this result indicates the reliability of the current method to calculate capture cross section. We applied this method for the ^{13}C(n,γ)^{14}C neutron capture reaction. Data for this reaction is available only below 100 keV. We estimated the contribution of the (non-resonant) direct capture reaction, which can be extended to a wider energy region. The obtained results is similar, but not exactly, the $1/v$ trend for the thermal energy. The contribution of this work was to obtain the spectroscopic factor for the investigated systems but also to shown the reliability of the potential model.

Bibliography

Arazi A., Abriola D., , 2023 Measurements of the Angular Distribution of Elastically and Inelastically Scattered Products. Springer Nature Singapore Singapore pp 99–130

Asplund M., Amarsi A. M., Grevesse N., The chemical make-up of the Sun: A 2020 vision, A&A, 2021, vol. 653, p. A141

Bertulani C. A., RADCAP: A potential model tool for direct capture reactions, Computer Physics Communications, 2003, vol. 156, p. 123

Burbidge E. M., Burbidge G. R., Fowler W. A., Hoyle F., Synthesis of the Elements in Stars, Rev. Mod. Phys., 1957, vol. 29, p. 547

Chamon L. C., Carlson B. V., Gasques L. R., Pereira D., De Conti C., Alvarez M. A. G., Hussein M. S., Cândido Ribeiro M. A., Rossi E. S., Silva C. P., Toward a global description of the nucleus-nucleus interaction, Phys. Rev. C, 2002, vol. 66, p. 014610

Clayton D. C., Principles of Stellar Evolution and Nucleosynthesis. The University of Chicago Press, 1968

Cristallo S., Cognata M. L., Massimi C., Best A., Palmerini S., Straniero O., Trippella O., Busso M., Ciani G. F., Mingrone F., Piersanti L., Vescovi D., The Importance of the 13C(,n)16O Reaction in Asymptotic Giant Branch Stars, The Astrophysical Journal, 2018, vol. 859, p. 105

de Jesús J., de Barbará E., Arazi A., Fernández Niello J., Martí G. V., Abriola D., Cardona M. A., Gollan F., Hojman D., Pacheco A. J., Samsolo N., ^{236}U identification in the new AMS beamline at the TANDAR accelerator. In Journal of Physics Conference Series , vol. 1291 of Journal of Physics Conference Series, 2019, p. 012001

Dey B., Bhattacharya S., , 2023 Experimental Details for a Typical Nuclear Physics Experiment. Springer Nature Singapore Singapore pp 25–58

Diehl R., Korn A. J., Leibundgut B., Lugaro M., Wallner A., Cosmic nucleosynthesis: A multi-messenger challenge, Progress in Particle and Nuclear Physics, 2022, vol. 127, p. 103983

Ertao L., Zhihong L., Yunju L., Shengquan G. B. Y., Jun S., Sheng Z., Youbao W., Gang L., Jiancheng L., Lin G., Qiwen F., Xinyue L., Yi S., Tianli M., Qi L., Shipeng H., Xin H., Huibin S., Yangping S., Yong Z., Zhiyu H., Changjin P., Weiping. L., Measurement of the Neutron Spectroscopic Factor in 10Be, Nuclear Physics Review, 2017, vol. 34, p. 446

Gamow G., Expanding Universe and the Origin of Elements, Phys. Rev., 1946, vol. 70, p. 572

Gollan Scilipotti F. D., Estudio del potencial de interacción de núcleos débilmente ligados, Universidad de Buenos Aires. Facultad de Ciencias Exactas y Naturales, 2019, PHD Thesis

Hammache F., de Séréville N., Transfer reactions as a tool in Nuclear Astrophysics, Frontiers in Physics, 2021, vol. 8, p. 630

Herndl H., Hofinger R., Jank J., Oberhummer H., Görres J., Wiescher M., Thielemann F. K., Brown B. A., Reaction rates for neutron capture reactions to C, N, and O isotopes to the neutron rich side of stability, Phys. Rev. C, 1999, vol. 60, p. 064614

Holt J. W., Whitehead T. R., , 2020 Modern Approaches to Optical Potentials. Springer Nature Singapore Singapore pp 1–30

Huang J., Bertulani C., Guimarães V., Radiative capture of nucleons at astrophysical energies with single-particle states, Atomic Data and Nuclear Data Tables, 2010, vol. 96, p. 824

Iben I. J., Renzini A., On the formation of carbon star characteristics and the production of neutron-rich isotopes in asymptotic giant branch stars of small core mass, ApJ, 1982, vol. 263, p. L23

Iliadis C., Nuclear physics of stars. Wiley, 2015

Krane S. K., Introductory Nuclear Physics. John Wiley Sons, 1988

Lee J., Tsang M. B., Lynch W. G., Neutron spectroscopic factors from transfer reactions, Physical Review C, 2007, vol. 75

Li Z. H., Li Y. J., Su J., Guo B., Li E. T., Dong K. J., Bai X. X., Li Z. C., Liu J. C., Yan S. Q., Wang Y. B., Zeng S., Lian G., Wang B. X., Jin S. J., Liu X., Zhang W. J., Huang W. Z., Fan Q. W., Gan L., Wu Z. D., Liu W. P., New determination of the proton spectroscopic factor in ^{9}Be from the ^{13}C(^{9}Be,^{8}Li)^{14}N angular distribution, Phys. Rev. C, 2013, vol. 87, p. 017601

Marzhan Nassurlla Buterbayev N., Karakozov B. K., Sakuta S. B., Boztozun I., Amangeldi N., New measurements and analysis of elastic scattering of ^{13}C by ^{9}Be nucleai in a wide enery range , Eur. Phys J. A, 2021, vol. 57

Mengoni A., Otsuka T., Ishihara M., Direct radiative capture of p-wave neutrons, Phys. Rev. C, 1995, vol. 52, p. R2334

Milner W. T., VAXPAK programs. Oak Ridge National Laboratory, 1986

Motobayashi T., Kohno T., Nakajima S., α Transfer Reactions Between Ligth Nuclei, Nuclear Physics A, 1979, vol. 331, p. 193

NRV, 2023 Nucleon Transfer Reaction http://nrv.jinr.ru/nrv./

Ohsaki T., Nagai Y., Igashira M., Shima T., Takeda K., Seino S., Irie T., New Measurement of the 12C(n, gamma) 13C Reaction Cross Section, ApJ, 1994, vol. 422, p. 912

Roy R. R., Nigam B. P., Nuclear Physics. Theory and Experiment. 1st ed. New York: John Wiley sons & Co Inc, 1968, 616 p.

Tarasov O. B., Bazin D., LISE++: Radioactive beam production with in-flight separators, Nuclear Instruments and Methods in Physics Research B, 2008, vol. 266, p. 4657

Terasawa M., Sumiyoshi K., Kajino T., Mathews G. J., Tanihata I., New Nuclear Reaction Flow during r-Process Nucleosynthesis in Supernovae: Critical Role of Light, Neutron-rich Nuclei, The Astrophysical Journal, 2001, vol. 562, p. 470

Thompson I. J., , Last update: 28th August 2006 FRESCO, Coupled Reaction Channels Calculation http://www.fresco.org.uk

Thompson I. J., Nunes F. M., Nuclear Reactions for Astrophysics. Cambridge University Press, 2009, 446 p.

Woosley S. E., Heger A., The evolution and explosion of massive stars, Reviews of Modern Physics, 2002, vol. 653

Appendix

Apêndice A

Fresco inputs for DWBA calculations

```
9be(13c,12c)10be @ 55 MeV;
NAMELIST
 &FRESCO hcm=0.03 rmatch=40 rintp=0.20 hnl=0.1 rnl=5.00 centre=0.0
jtmin=0.0 jtmax=120 absend=-1.0
thmin=0.00 thmax=90.00 thinc=1.00
iter=1 nnu=36
chans=1 xstabl=1
elab=55.0 /
&PARTITION namep='c13' massp=13. zp=6 namet='be9' masst=9. zt=4 nex=1 /
&STATES jp=0.5 bandp=-1 ep=0.0 cpot=1 jt=1.5 bandt=-1 et=0.0000 /

&PARTITION namep='c12' massp=12. zp=6 namet='be10' masst=10. zt=4
qval=1.865884801 nex=1 /
&STATES jp=0.0 bandp=1 ep=0.0 cpot=2 jt=0.0 bandt=-1 et=0.0000 /
&partition /

&POT kp=1 ap=13.000 at=9.000 rc=1.25/
&POT kp=1 type=1 p1=175.0 p2=0.8 p3=0.778 p4=25.2 p5=1.25 p6=0.522 /

&POT kp=2 ap=12.000 at=10.000 rc=1.20 /
&POT kp=2 type=1 p1=33.69 p2=0.97 p3=0.92 p4=6.52 p5=1.51 p6=0.48 /

&POT kp=3 at=9 rc=1.25 /
```

```
&POT kp=3 type=1 p1=50.00 p2=1.2 p3=0.65 /

&POT kp=4 at=10 rc=1.25 /
&POT kp=4 type=1 p1=50.00 p2=1.2 p3=0.65 /

&POT kp=5 ap=13.000 at=10.000 rc=1.20 /
&POT kp=5 type=1 p1=33.69 p2=0.97 p3=0.92 p4=6.52 p5=1.51 p6=0.48 /
&pot /

&Overlap kn1=1 ic1=1 ic2=2 in=1 kind=0 nn=1 l=2 sn=0.5 ia=1 ib=1 j=0.5
kbpot=3 be=4.9464 isc=1 ipc=0 /
&Overlap kn1=2 ic1=2 ic2=1 in=2 kind=3 nn=1 l=1 sn=0.5 ia=1 ib=1 j=1.5
kbpot=4 be=6.8124 isc=1 ipc=0 /
&overlap /

&Coupling icto=-2 icfrom=1 kind=7 ip1=0 ip2=-1 ip3=5 /
&CFP in=1 ib=1 ia=1 kn=1 a=1.2570/
&CFP in=2 ib=1 ia=1 kn=2 a=0.95 /
&CFP /
&coupling /
```

```
9be(13c,14c)8be @ 55 MeV;
NAMELIST
 &FRESCO hcm=0.03 rmatch=40 rintp=0.20 hnl=0.1 rnl=5.00 centre=0.0
jtmin=0.0 jtmax=120 absend=-1.0
thmin=0.00 thmax=90.00 thinc=1.00
iter=1 nnu=36
chans=1 xstabl=1
elab=55.0 /
&PARTITION namep='c13' massp=13. zp=6 namet='be9' masst=9. zt=4 nex=1 /
&STATES jp=0.5 bandp=-1 ep=0.0 cpot=1 jt=1.5 bandt=-1 et=0.0000 /
&PARTITION namep='c14' massp=14. zp=6 namet='be8' masst=8. zt=4
qval=6.51108 nex=1 /
&STATES jp=0.0 bandp=1 ep=0.0 cpot=2 jt=0.0 bandt=1 et=0.0000 /
&partition /

&POT kp=1 ap=13.000 at=9.000 rc=1.25 /
&POT kp=1 type=1 p1=175 p2=0.8 p3=0.778 p4=25.2 p5=1.25 p6=0.522 /

&POT kp=2 ap=14.000 at=8.000 rc=1 /
&POT kp=2 type=1 p1=76 p2=0.92 p3=0.77 p4=28 p5=1.29 p6=0.415 /

&POT kp=3 at=9 rc=1.25 /
&POT kp=3 type=1 p1=30 p2=1.25 p3=0.65 /

&POT kp=4 at=14 rc=1.25 /
&POT kp=4 type=1 p1=30 p2=1.25 p3=0.65 /

&POT kp=5 ap=13.000 at=8.000 rc=1.0 /
&POT kp=5 type=1 p1=175 p2=0.8 p3=0.778 p4=25.2 p5=1.25 p6=0.522 /
&pot /

&Overlap kn1=1 ic1=1 ic2=2 in=1 kind=0 nn=1 l=1 sn=0.5 ia=1 ib=1 j=0.5
```

```
kbpot=3 be=8.17647 isc=1 ipc=0 /
&Overlap kn1=2 ic1=2 ic2=1 in=2 kind=3 nn=1 l=1 sn=0.5 ia=1 ib=1 j=1.5
kbpot=4 be=1.66539 isc=1 ipc=0 /
&overlap /

&Coupling icto=-2 icfrom=1 kind=7 ip1=0 ip2=-1 ip3=5 /
&CFP in=1 ib=1 ia=1 kn=1 a=0.670820 /
&CFP in=2 ib=1 ia=1 kn=2 a=1.10 /
&CFP /
&coupling /
```

Apêndice B

RADCAP inputs for neutron capture calculations

```
*****************************************************************
*   ********    Input of program DICAP  *******
* 12C(0+)+n(1/2+)=13C(1/2-)
* IOPT   = option for potentials: 1 (2) for Woods-Saxon (M3Y)
* NPNTS = no. of integration points in radial coordinate ( < 10000)
* RMAX = maximum radius size (< 250 fm).
* NEPTS = number of points in energy ( < 1000)
*
* IOPT    NPNTS    RMAX     NEPTS
*
  1       9999     250       200
*
* N_0  =  nodes of the G.S. wave function
* AIA  =  spin of the particle A (core)
* AIB  =  intrinsic spin of the particle B
* AIC  =  total angular momentum of the ground state of C = A + B
*         (channel spin)
* J0   =  single-particle angular momentum
* L0   =  orbital angular momentum
* EBOUND = binding energy of the ground state (absolute value)
*
* N_0    AIA     AIB     AIC     AJ0      L_0      EBOUND
*
```

```
  0      0       0.5     0.5     0.5      1         4.94635
*
* JOPT = 1 (0) if final state ang. mom., AICF, is (is not) to be
*        summed over all possible values. If JOPT=1, AICF  can be
*        entered as any value.
* AICF =  spin of the excited state after all ang. mom. coupling
*         (channel spin)
*
* JOPT     AICF
*
  1         1
*
* Z1, Z2 = charges of the nuclei
* A1, A2 = masses of the nuclei (in nucleon mass units)
*
* Z1      A1     Z2     A2
*
   0       1      6     12
*
* V0   =  depth of central potential
* R0   =  radius of the central potential
* AA   =  diffuseness of the central potential
* VS0  =  depth of spin-orbit potential
* RS0  =  radius of the spin-orbit potential
* AAS  =  diffuseness of the spin-orbit potential
* RC   =  Coulomb radius (usually, RC = R0)
*---------------------------------------------------------------
*  WS  =  V_0 f(r,R0,AA) - V_S0 (l.s) (r_0^2/r) d/dr f(r,RS0,AAS)
*
*  f(r,R0,a) = [ 1 + exp((r-R_0)/a) ]^(-1)
*
*  r_0 = 1.4138 fm is the Compton wavelength of the pion.
```

```
* (if IOPT=2 insert a "*" at the input line)
*-----------------------------------------------------------------
* V0        R0       AA     VS0     RS0      AAS     RC
*
  -14.75    2.86    0.62   -7.00    2.86     0.62    2.86
*
* If IOPT = 2, or else (but not 1), enter FC, FSO and RC:
*    (in this case, insert a '*' sign in above row, or delete it)
* FC      = multiplicative factor of central part of M3Y potential
* FSO     = multiplicat. factor of spin-orbit part of M3Y potential
* RC      =  Coulomb radius
* (if IOPT=1 insert a "*" at the input line)
*
*  FC        FSO       RC
*   1.5       0.2       2.391
*
* EI,EF =  initial relative energy, final relative energy
*
* EI       EF
*
  0.       0.1
*
* NS1,NP1,NP3,ND3,ND5,NF5,NF7 = (1) [0] for  inclusion (no inclusion)
*     of  s1/2, p1/2, p3/2, d3/2, d5/2, f5/2, and f7/2  partial waves
*
*  NS     NP1     NP3     ND3    ND5    NF5    NF7
*
   1       0        0      1      1      0      0
*
* MP   = multipolarity: 0 (M1),  1 (E1),   2 (E2)
* SF   = Spectroscopic factor
*
```

```
*  MP         SF
*
   1         0.9025
*
* GA  = magnetic moment (in units of the nuclear magneton) of
*        particle A (core)
* GB  = magnetic moment of particle B (proton, neutron, alpha, etc.)
*
*   GA          GB
*
    0        -3.826
*
**********************************************************************
```

```
*****************************************************************
*   ********    Input of program DICAP  *******
*
*13C(1/2-)+n(1/2+)=14C(0+)
*
* IOPT   = option for potentials: 1 (2) for Woods-Saxon (M3Y)
* NPNTS = no. of integration points in radial coordinate ( < 10000)
* RMAX = maximum radius size (< 250 fm).
* NEPTS = number of points in energy ( < 1000)
*
* IOPT    NPNTS    RMAX     NEPTS
*
  1       9999     250.      200
*
* N_0  =  nodes of the G.S. wave function
* AIA  =  spin of the particle A (core)
* AIB  =  intrinsic spin of the particle B
* AIC  =  total angular momentum of the ground state of C = A + B
*         (channel spin)
* J0   =  single-particle angular momentum
* L0   =  orbital angular momentum
* EBOUND = binding energy of the ground state (absolute value)
*
* N_0    AIA     AIB     AIC     AJ0      L_0      EBOUND
*
  0      1.5     0.5      0       1.5      1       8.17647
*
* JOPT = 1 (0) if final state ang. mom., AICF, is (is not) to be
*        summed over all possible values. If JOPT=1, AICF  can be
*        entered as any value.
* AICF =  spin of the excited state after all ang. mom. coupling
*         (channel spin)
```

```
*
* JOPT     AICF
*
  1         1
*
* Z1, Z2 = charges of the nuclei
* A1, A2 = masses of the nuclei (in nucleon mass units)
*
* Z1      A1     Z2     A2
*
   0      1      6      14
*
* V0   =  depth of central potential
* R0   =  radius of the central potential
* AA   =  diffuseness of the central potential
* VS0  =  depth of spin-orbit potential
* RS0  =  radius of the spin-orbit potential
* AAS  =  diffuseness of the spin-orbit potential
* RC   =  Coulomb radius (usually, RC = R0)
*--------------------------------------------------------------------
*  WS  =  V_0 f(r,R0,AA) - V_S0 (l.s) (r_0^2/r) d/dr f(r,RS0,AAS)
*
*  f(r,R0,a) = [ 1 + exp((r-R_0)/a) ]^(-1)
*
*  r_0 = 1.4138 fm is the Compton wavelength of the pion.
* (if IOPT=2 insert a "*" at the input line)
*--------------------------------------------------------------------
* V0        R0       AA     VS0     RS0      AAS     RC
*
  -15.02   2.94     0.62   -7.0    2.94     0.62    2.94
*
* If IOPT = 2, or else (but not 1), enter FC, FSO and RC:
```

```
*    (in this case, insert a '*' sign in above row, or delete it)
* FC      = multiplicative factor of central part of M3Y potential
* FSO     = multiplicat. factor of spin-orbit part of M3Y potential
* RC      =  Coulomb radius
* (if IOPT=1 insert a "*" at the input line)
*
*  FC        FSO       RC
*   1.5       0.2       2.391
*
* EI,EF =  initial relative energy, final relative energy
*
* EI       EF
*
  0        0.1
*
* NS1,NP1,NP3,ND3,ND5,NF5,NF7 = (1) [0] for  inclusion (no inclusion)
*     of  s1/2, p1/2, p3/2, d3/2, d5/2, f5/2, and f7/2  partial waves
*
*  NS     NP1     NP3     ND3    ND5    NF5    NF7
*
   1       0       0       1      1      0      0
*
* MP   = multipolarity: 0 (M1),  1 (E1),   2 (E2)
* SF   = Spectroscopic factor
*
*  MP        SF
*
   1         1.21
*
* GA  = magnetic moment (in units of the nuclear magneton) of
*        particle A (core)
* GB  = magnetic moment of particle B (proton, neutron, alpha, etc.)
```

```
*
*   GA          GB
*
     0       -3.826
*
**********************************************************************
```